WILEY-VCH

Realizing High-Energy and Stable Wire-Type Batteries with Flexible Lithium Metal Composite Yarns

Yuan Gao, Hong Hu, Jian Chang, Qiyao Huang, Qiuna Zhuang, Peng Li, and Zijian Zheng*

Dr. Y. Gao, Dr. H. Hu, Dr. J. Chang, Dr. Q. Huang, Q. Zhuang, Dr. P. Li, Prof. Z. Zheng

Laboratory for Advanced Interfacial Materials and Devices, Research Centre for Smart Wearable Technology, Institute of Textiles and Clothing, The Hong Kong Polytechnic University, Hong Kong SAR, China.

Prof. Z. Zheng

Research Institute for Smart Energy, The Hong Kong Polytechnic University, Hong Kong SAR, China.

E-mail: tczzheng@polyu.edu.hk

Abstract

High-capacity and omnidirectionally flexible wire-type lithium (Li) metal batteries represent a feasible technology for the realization of electronic textiles. However, the use of commercially available Li metal wire as anodes nowadays confronts many electrochemical and mechanical issues such as dendrites formation, low yield strength, and poor fatigue resistance. Here we design a flexible and stable Li metal composite yarn (LMCY) via a fast capillary filling of molten Li into metallic carbon yarn for fabricating high-energy-density and long-lasting wire-type LMBs. LMCY shows outstanding electrochemical cyclic stability, mechanical strength, flexibility and durability. Pairing lithium iron phosphate (LFP) with the LMCY as anode results in a foldable LFP||Li full cell that delivers a high energy density over 290 Wh L^{-1} and a long lifetime over 800 cycles with a capacity retention of over 50% after 750 charge/discharge cycles. We demonstrate the seamless integration of this wire-shape LFP||Li cell with commercial textiles as a built-in power supply to wearable electronics, while maintaining the excellent breathability of the textiles. LMCYs are also adaptable to other high-performance wire-type batteries, such as lithium-sulfur battery.

1. Introduction

Electronic textiles (E-textiles) that integrate the state-of-the-art electronic devices such as sensors,[1] transistors,[2] actuators,[3] and displays[4] with consumer clothing are deemed as the ultimate form of wearables. They are foreseen to bring enormous convenience to our daily life by offering body-worn protection,[5] communication,[6] navigation,[7] and healthcare.[8] However, the persistent powering of e-textiles is still challenging because of the difficulty in developing matched flexible and high-performance batteries as the fundamental constituent of the e-textiles.[9] Existing coin and pouch types of batteries remain the most widely used options nowadays, but their fixed shapes and rigidity largely hinder the seamless integration into different wearable formats, particularly those require high levels of deformation and wearing comfort.[10]

Wire-type batteries appear to be promising candidates to address this challenge because the omni-directional flexibility offered by the wire shape can effectively withstand complicated mechanical deformations, and the resemblance of the shape to slender fibers and yarns of textiles allows for the easy integration into wearable formats via mature textile technologies, such as braiding, weaving, and knitting.[11]

To date, only a few studies of wire-type batteries have been reported in the literature, most of which are developed on the basis of lithium-ion battery (LIB) and zinc-ion battery (ZIB) chemistries. Nevertheless, due to the low theoretical capacity and the low mass loading of the anode materials, the energy densities of those wire-type LIBs and ZIBs are low (5–160 Wh L^{-1}).[12-19] Recent studies on lithium (Li) metal anode have suggested that wire-type Li metal batteries (LMBs) may meet the energy demand because of the remarkable theoretical capacity and the lowest electrochemical potential of Li.[20] However, those reports only made use of bulky and thick Li metal wires (LMWs) in their study, which adversely resulted in two major disadvantages. Electrochemically, LMWs showed a short cyclic life (3–100 cycles) owing to the formation of Li dendrites, and the largely oversized Li metal led to the low energy density

of the battery (2–70 Wh L^{-1}).[21-24] Mechanically, LMWs could easily undergo plastic deformation because of its low yield strength (<1 MPa), which significantly limited the flexing stability of the wire-type battery.[25, 26]

It is noted that, in the literature studies of flexible LMBs, the cycling stability and flexibility of Li metal anodes can be substantially enhanced by depositing the Li metal on a flexible host. However, these studies adopted the reactive wetting process for the fabrication of Li metal composites, which required the use of Li-reactive materials.[27-32] On one hand, the molten Li must react with oxides or form new alloys with reactive metals before it can wet the hosts. Such vigorous chemical reactions are likely to damage the micro/nanostructures of the hosts.[27, 33] On the other hand, the as-generated Li oxides (Li$_2$O), if not removed properly, can hamper the infusion process and reduce the purity, capacity, as well as the electrochemical stability of as-fabricated Li metal composites.[31, 34]

Herein, we report the first study of highly flexible and electrochemically stable Li metal composite yarn (LMCY), in which Li metal is composited with copper-coated carbon (Cu-C) yarn via the fast capillary filling, a non-reactive wetting process without the use of Li-reactive materials. In such a process, molten Li can spontaneously wet the surface of Cu-C yarn and infuse into the interspace of the yarn, benefiting from the good lithiophilicity and the unique structure of the yarn. LMCY possesses a high linear capacity of 1 mAh cm^{-1} and shows much lower overpotential and enhanced electrochemical cycling stability than LMW. Additionally, the yield strength of LMCY is ~10 folds higher than LMW, which leads to outstanding mechanical flexibility and durability. We demonstrate the fabrication of wire-type LMBs by pairing the LMCY anode with lithium iron phosphate (LFP) or sulfur (S) cathode. The LFP||LMCY cells can deliver a record-breaking volumetric energy density of ~293 Wh L^{-1}, a long lifetime over 800 cycles with a capacity retention of over 50% after 750 charge/discharge cycles, and an outstanding foldability. The S||LMCY cells also achieve a volumetric energy density of ~145 Wh L^{-1}, which is ~7 folds higher than the reported wire-type S||Li cells. At last,

we weave these wire-type LMBs with common textile yarns to create flexible and permeable body-worn power fabrics.

2. Results and Discussion

2.1. Fabrication and characterization of LMCY

LMCY was fabricated via infusion of molten Li into the flexible and lithiophilic Cu-C yarn (**Figure 1**a). The pristine C yarn was a twist of ~200 C fibers of 10 μm each in diameter (Figure S1a and b), which was naturally flexible and could provide enough capillarity to liquids that wet its surface. However, the large contact angle ~120° of the molten Li on the C substrate indicated the lithiophobic nature of the C yarn (Figure 1b). In contrast, the small contact angle of ~30° of the molten Li on the Cu substrate indicated a good lithiophilicity. To render the C yarn lithiophilic, we coated C yarn with Cu via the method of polymer-assisted metal deposition (PAMD),[35, 36] which resulted in a uniform coating of Cu (~200 nm thick) on each C fiber (Figure S1c). The molten Li could easily wet the Cu-C yarn once contact, and quickly infused into the yarn due to the great capillary force to form the LMCY (Figure 1c and d).

Scanning electron microscopy (SEM) characterized the morphological change of Cu-C yarn during the infusion process. The molten Li filled the gaps among neighboring Cu-C fibers (Figure 1e–g). The resultant LMCY pertained the geometrical structure of the Cu-C yarn with all the Cu-C fibers embedded in the Li metal (Figure 1h and i, Figure S2). Since the infusion process was performed at 623 K, no intermetallic bonds between Cu and Li shall form according to their phase diagram (Figure 3a). X-ray diffraction spectroscopy (XRD) confirmed the well-retained diffraction peaks of Cu at 43° and 50.4° and the appearance of the new diffraction peaks of Li at 36.2° and 52.3° (Figure S3b). These results suggested that the infusion of molten Li into Cu-C yarn was essentially a capillary filling without the formation of oxides or intermetallic compounds.

In most of the previous studies, metal oxides were used as the Li-reactive materials for the infusion of molten Li.[27, 28, 37] The reaction between the molten Li and metal oxides is described below:

$$M_xO_y + 2yLi(l) = xM + yLi_2O \quad (\Delta G < 0) \quad (1)$$
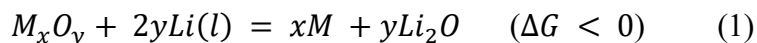
where M_xO_y refers to metal oxides such as manganese dioxide (MnO_2)[27] and zinc oxide (ZnO)[28], and M represents metal. The chemical reaction between the molten Li and these metal oxides normally generated a large amount of Li_2O, which shall deteriorate the infusion speed of Li. For illustration, we compared the infusion process between the Cu-C and CuO-coated C (CuO-C) yarns, where the CuO-C yarn was prepared by thermal oxidation of Cu-C yarn in the air (Figure S4a). The infusion of molten Li into CuO-C yarn exhibited a low speed of 32 cm min^{-1}, owing to the formation of Li_2O as the new interface between molten Li and the host. The vigorous chemical reaction between CuO and molten Li further reduced the dense CuO film into discrete Cu particles (Figure S4b and c, Figure S5a, Movie S1).[33, 38] In contrast, the infusion of molten Li into Cu-C yarn showed a high speed of 70 cm min^{-1} without negative impact on the host structure (Figure S5b, Movie S2). As such, we demonstrated a 10-meter-long LMCY with remarkable flexibility in less than 15 mins (Figure 1j–l).

2.2. Simulation study of the infusion process

To gain a better understanding of the infusion process, a simulation on the basis of Two-Phase Flow and Level Set[39] was developed to study the infusion of molten Li into different hosts including Cu-C yarn, CuO-C yarn, and C yarn (refer to the details in Experimental Section). It should be noted that both the chemical reaction and the wetting process occurred very fast in a reactive wetting process, thus it was less likely to clearly differentiate them by their orders. As such, we assumed the oxidation of molten Li by CuO (formation of Li_2O) occurred ahead of the infusion process because of the high reactivity of molten Li with CuO.

In this scenario, the infusion into CuO-C yarn was deemed as the flow of molten Li into Li_2O-C yarn. The contact angles of molten Li on the surface of Cu, Li_2O,[38] and C were ~30°, ~80°, and ~120°, respectively. The geometry of the yarns consisted of multiple parallel fibers with the diameter of 10 μm and the interspace of 5 μm (**Figure 2**a, d, g).

Figure 2 displayed the morphological evolution of the interface between the molten Li and argon (Ar) atmosphere on different substrates. On Cu-C, the molten Li creeped along the fiber and deformed the flat interface of Li/Ar into the concave meniscus at t_1 (Figure 2b). Ideally, the meniscus possessed a radius of curvature of r. The morphological change of the interface of Li/Ar created a Laplace pressure ($P \propto 1/r$) pointing to the Ar, which could drive the infusion of the molten Li into the interspace of neighboring Cu-C fibers at t_2 (Figure 2c). In comparison, the meniscus trapped in the Li_2O-C fibers showed a larger r than that of Cu-C fibers (Figure 2e), which resulted in a smaller P across the interface of Li/Ar and thus a slower infusion speed (Figure 2f). The average infusion velocity of molten Li into the Cu-C yarn was over two folds of that of the Li_2O-C yarn ($d_1/d_2 \approx 2.5$), which was in a good agreement with our experimental result. The interface of Li/Ar on unmodified C fibers showed a convex meniscus because of the lithiophobicity of C (Figure 2h). The Laplace pressure generated by the deformation of Li/Ar interface pointed to the molten Li, which repelled the infusion of the molten Li into the C yarn (Figure 2i).

2.3. Electrochemical performances of LMCY

To date, carbonaceous materials were the most used current collectors in wire-type batteries, yet their electrical conductivity were low.[21, 40] This drawback led to the high ohmic loss of the battery electrodes.[41] To quantify the ohmic loss of the electrodes (U_{AB}), we derived the following equation from the equivalent circuit of the wire-type symmetric cells (**Figure 3**a and b):

$$U_{AB} = \frac{L^2}{2} iR \quad (2)$$

where *L* is the length of the electrode, *i* is the current density, *R* is the linear resistance of the current collector (refer the detailed derivation in Experimental Section). According to equation (2), the use of Cu-C yarn could significantly reduce the ohmic loss of the electrode, as Cu-C yarn exhibited much lower linear resistance (~1 Ω cm^{-1}) than those carbonaceous materials (e.g., ~20 Ω cm^{-1} for the C yarn). As proof-of-concept, the overpotentials of symmetric cells made of a pair of LMCYs with different lengths (1 cm, 2 cm, 4 cm, and 6 cm) were tested (Figure 3c). At the current densities of 15 μA cm^{-1}, 25 μA cm^{-1}, 50 μA cm^{-1}, and 100 μA cm^{-1}, the cells with different lengths of LMCY exhibited similar overpotentials, being ~40 mV, ~47 mV, ~67 mV, and ~94 mV, respectively. These results confirmed the small ohmic loss of LMCY, owing to the use of highly conductive Cu-C yarn.

We obtained the linear capacity of LMCY by fully stripping the Li from LMCY. During such a process, Li was stripped from one donating LMCY and plated on the adjacent surface of the opposite LMCY (Figure S6a and b). The Cu-C fibers were fully exposed when all the Li was stripped from the donating LMCY (Figure S6c). The linear capacity of LMCY (~1 mAh cm^{-1}) was much higher than the Li composite yarn using CuO-C as the host (~0.8 mAh cm^{-1}) (Figure 3d). We also conducted long-term stripping and plating of Li at different current densities and depths of discharge (DoDs), so as to evaluate the electrochemical stability of LMCY (Figure S7, Figure S8). Particularly, LMCY could stably run for more than 1,000 hrs at a current density of 50 μA cm^{-1} and a DoD of 10% (~0.1 mAh cm^{-1}) (Figure 3e). When the current density and DoD increased to 100 μA cm^{-1} and 50% (~0.5 mAh cm^{-1}), respectively, LMCY still exhibited a stable overpotential of ~94 mV for more than 400 hrs (Figure 3f). In comparison, LMW presented much higher overpotentials and shorter cyclic life than LMCY under the same testing conditions (Figure S9). For instance, LMW displayed a high overpotential of ~200 mV and only run for less than 80 hrs (<8 cycles) at a current density of

100 µA cm^{-1} and a DoD of 50%. The low overpotentials and good electrochemical stability of our LMCY also outperformed the previously reported fiber-shaped Li metal anode prepared via the reactive wetting process. For instance, when using the ZnO-coated carbon nanotubes (CNTs) as the scaffold, the fiber-shaped Li metal anode rendered a high overpotential of ~200 mV at the current density of 100 µA cm^{-1}, and can only run for 40 hrs.[31]

In order to explain the good electrochemical stability of LMCY, we performed the postmortem investigation in the morphologies of LMW and LMCY during the long-term plating and stripping of Li. Initially, both LMCY and LMW showed smooth surfaces (Figure S10a and b). After the cycling test, clusters of Li particles were generated on the LMW (Figure 10c and d). At a high current density and a large DoD, these particles evolved into the dendrite-like morphology (Figure S10e), which was believed to cause the failure of the cell through penetration of the separator and short connection of the electrodes. On the contrary, the Cu-C yarn effectively suppressed the formation of Li dendrites, which could be ascribed to the reduction of the localized current densities and the energy barrier for the nucleation of Li (Figure S10f).[42]

In brief, the improvement of the above electrochemical performances can be ascribed to the use of unique Cu-C yarns as the current collectors for the fabrication of stable LMCYs: i) Compared to the previous reports that using carbonaceous materials as the fiber-shaped current collectors, Cu-C yarns render a much higher electrical conductivity, which endows the wire-type symmetric cells with a largely reduced ohmic loss; ii) The use of porous Cu-C yarns can reduce the localized current density, benefiting for the LMCYs to achieve a small overpotential and stable SEI; iii) The porous structure of Cu-C yarns can also accommodate the deposition of Li, and lead to a smooth surface of LMCY during charge/discharge test (Figure S11).

2.4. Flexibility of LMCY

LMWs underwent plastic deformations easily due to their low yield strain (<0.2%) and yield strength (<1 MPa). In comparison, LMCYs possessed a much higher yield strength (~9 MPa) than LMWs, making them less likely to break when the same stress is applied (**Figure 4**a). Figure 4b showed the overpotentials of two types of symmetric cells (using LMCYs and LMWs) under different bending radii. In particular, the cell using LMCYs delivered a negligible change of overpotentials with the decrease of bending radius. However, the overpotential of the cell using LMWs drastically increased from ~170 mV to ~330 mV at the flexing radius of 3 mm. The mechanical durability of both types of cells were also evaluated. The cell using LMCYs rendered a stable overpotential after repeatedly flexed for 150 cycles at a flexing radius of 1 mm. In a stark contrast, the cell using LMWs exhibited erratic fluctuation of overpotentials after only a few tens of bending cycles due to the fracture of LMWs (Figure 4c, Figure S12).

We further developed a finite element analysis (FE) to investigate the significant difference of the flexibility between LMCY and LMW. The LMW was set as a Li cylinder of 100 μm in diameter and 0.5 mm in length (Figure 4d, Q1), while the LMCY consisted of 32 twisted Cu-C fibers of 10 μm each in diameter that were embedded in a Li cylinder of the same size (Figure 4d, R1). Equal and opposite bending angles were applied simultaneously on the two ends of the cylinder, so as to observe the different crack behaviours between LMCY and LMW (see the details of the FE simulation in Experimental Section). When subjected to the multiple flexure at a large bending radius (e.g., 3 mm), a large crack occurred on the surface of LMW (Figure 4d, Q2). The crack propagated with the decrease of bending radius and repeated flexure, and finally resulted in the complete fracture of LMW (Figure 4d, Q3 and Q4). In contrast, bending the LMCY initially resulted in tiny cracks of Li (Figure 4d, R2). At a small bending radius (e.g., 1 mm), these cracks were confined in the upper part of LMCY, as the elastoplastic Cu-C yarn could dissipate the strain and inhibit the propagation of the cracks (Figure 4d, R3 and R4). The well retained structural integrity of LMCY could explain the

negligible change of the electrode conductivity and the stable overpotentials in the mechanical durability test.

2.5. Fabrication and electrochemical performances of wire-type LMBs

We fabricated yarn-like LFP or S cathodes and then paired them with the LMCY anode to yield wire-type LMBs (**Figure 5**a). We first fabricated nickel-coated C (Ni-C) yarn to serve as the current collector of yarn-like cathodes (Figure S13a and b). LFP or S slurry was then dipped coated onto the Ni-C yarn, followed by placing in a vacuum oven to allow sufficient penetration of the active materials into the internal space of the yarn (Figure S13c–e). In a typical wire-type LMB, the cathode and anode were aligned in parallel, electrically isolated by a polypropylene separator and encapsulated in a polyolefin tube (Figure 5b).

We first compared the cycling performances between LFP||LMCY and LFP||LMW. At a mass loading of ~0.25 mg cm^{-1} and a current density of 25 μA cm^{-1} (~0.5 C), LFP||LMCY delivered an initial specific capacity of ~150 mAh g^{-1} and showed high capacity retention of 76% and 50% after charge/discharge for 400 and 784 cycles, respectively (Figure 5c). When the current density increased to 100 μA cm^{-1}, LFP||LMCY still stably run for more than 400 cycles (Figure S14a). The LFP||LMW battery, however, presented much higher voltage hysteresis, lower specific capacity and shorter cyclic life (Figure S14b–e). When increasing the mass loading of LFP to ~1.2 mg cm^{-1}, the linear capacity of LFP||LMCY was enhanced from 37.3 μAh cm^{-1} to 150.9 μAh cm^{-1} at the current density of 25 μA cm^{-1} (~0.15 C), which kept a high retention of 88% after 170 cycles. Even at a high current density of 100 μA cm^{-1}, the battery still reserved a linear capacity of 68.3 μAh cm^{-1}, and stably run for more than 170 cycles (Figure 5d and Figure S15). The electrochemical impedance of LFP||LMCY before and after cyclic test was also provided (Figure S16). The slightly increased charge transfer impedance after cyclic test indicated the gradual exhaustion of the electrolyte, which can be used to explain the capacity decay of LFP||LMCY after long-term cyclic test. The linear capacity of

LFP‖LMCY can be further increased with the use of multiply yarns as the cathodes. As a proof of concept, three-ply carbon yarns were simply braided and coated with Ni to render a larger surface area for a higher loading amount of LFP (Figure S17). The battery using the braided LFP cathode yarn thus delivered an enhanced linear capacity of 210 μAh cm^{-1} (Figure S18). Noteworthy, LFP‖LMCY obtained a record-breaking volumetric energy density of 292.4 Wh L^{-1} (normalized to the volumes of cathode, anode, and current collectors) and the longest cycle life among the previously reported wire-type LMBs (Figure 5e and Table 1).[21-24, 31, 43] The energy density of LFP‖LMCY also outperformed other types of batteries (Table S1).[12-15, 40, 44-46]

Importantly, LFP‖LMCY could be readily bent, folded, or even knotted, while persistently powered 36 yellow LEDs for tens of minutes (Figure 5f). The realization of flexible, durable, and wearing comfortable e-textiles requires the seamless integration of matched batteries. We thus weaved LFP‖LMCY with cotton yarns to create the fully flexible and permeable body-worn power fabrics. The battery textile consisted of six LFP‖LMCY that were electrically connected in parallel (Figure 5g), which could deliver an areal capacity of ~1 mAh cm^{-2} (Figure 5h). We further demonstrated a battery glove by seamlessly embedding the LFP‖LMCY along the seam line of each glove finger (Figure 5i). The battery glove showed a stable power delivery without interruption by the natural motion of human body, demonstrating its great capability in the application of flexible and wearable electronics (Movie S3). The air resistance and water vapor permeability of the power fabrics were 0.81 kPa sm^{-1}, and 29 gh^{-1}m^{-2}, respectively, which were similar to those of commercial cotton fabrics (0.7 kPa sm^{-1} and 35.8 gh^{-1}m^{-2}, respectively). Since the trans epidermal water loss from human skin ranged from 5.6 gh^{-1}m^{-2} to 18.7 gh^{-1}m^{-2} under indoor conditions,[47] the high permeability of the power fabrics allowed sufficient perspiration and ensured the good wearing comfort (Figure S19).

For S‖LMCY, we obtained a highest linear capacity of ~120 μAh cm^{-1}, translating into a volumetric energy density of 144.7 Wh L^{-1}. The battery could endure tens of charge/discharge

cycles at different current densities and DoDs (Figure S20), which are also superior to those reported wire-type S∥Li batteries using LMWs.[21, 43] The S∥LMCY showed a typical capacity decay during the initial ten charge/discharge cycles, which was associated with the common dissolution of soluble polysulfide species (Li_2S_n, n ≥ 4).[48] After that, S∥LMCY delivered a stable discharge voltage of ~2.1 V and capacity over another 30 charge/discharge cycles, during which battery was bent 100 times (Figure S21).

3. Conclusion

We have realized the infusion of molten Li into Cu-C yarn via the fast capillary filling, a non-reactive wetting process. The new fabrication route circumvented the use of Li-reactive materials, which substantially brought in several significant advances, including rapid and scalable preparation, well-retained host structure, and further enabled the high-capacity, impurity-free, flexible and stable LMCYs. The LMCY displayed a yield strength, ~10 folds higher than that of LMW, and showed a dendrite-free morphology when it was cycled at different current densities and DoDs. As such, wire-type LMBs made by paring LMCYs with yarn-like LFP or S cathodes, could readily achieve a record-breaking volumetric energy density of ~293 Wh L^{-1}, a long lifetime over 800 cycles with a capacity retention of over 50% after 750 charge/discharge cycles, and good foldability. These high-performance wire-type batteries were seamlessly integrated into the body-worn power fabrics, which offered high air and water vapor permeability to ensure wearing comfort as well as stable energy supply to electronic devices. The design rationale of the composite electrodes, in principle, is applicable to a variety of anodic and cathodic materials used for batteries and supercapacitors for the realization of durable, flexible, and wearing-comfortable e-textiles.

4. Experimental Section

Preparation of copper/nickel-coated carbon yarns: The copper/nickel-coated carbon (Cu-C/Ni-C) yarn was prepared by depositing a layer of Cu or Ni onto the C yarn via the process of PAMD. Firstly, the pristine C yarn was activated in a mixture of concentrated sulfuric acid/nitric acid with vigorous ultrasonication at 353 K and rinsed with deionized (DI) water. Then, the acid-treated C yarn was silanized in the solution containing 4 ml (3-(methacryloyloxy) propyl) trimethoxysilane solution, 95 ml ethanol, 4 ml acetic acid and 1 ml DI water for 1 hr at room temperature. After thoroughly rinsed with DI water, the silanized C yarn was further immersed in a mixture of (2-(methacryloyloxy)ethyl)trimethyl ammonium chloride (METAC) (20% v/v in water) and potassium persulfate (2 g L^{-1}) to perform the polymerization at 353 K for 1 hr. After that, PMETAC-coated C yarn was immersed into a 5 mM ammonium tetrachloropalladate ($(NH_4)_2PdCl_4$) solution for 30 mins in a dark environment for ion exchange, so as to load enough $(PdCl_4)^{2-}$. Then, $(PdCl_4)^{2-}$-loaded C yarn was put into the electroless deposition bath (ELD) for a specific time for deposition of Cu or Ni. The as-prepared Cu-C/Ni-C yarn was finally heated at the temperature of 673 K in an argon (Ar)-filled glove box to remove the surface oxides. The ELD bath of Cu is a mixture of 1:1 (v/v) of solution A and B. The solution A contains sodium hydroxide (NaOH) (12 g L^{-1}), copper (II) sulfate pentahydrate ($CuSO_4 \cdot 5H_2O$) (13 g L^{-1}), and potassium sodium tartrate tetrahydrate ($KNaC_4H_4O_6 \cdot 4H_2O$) (29 g L^{-1}) in DI water. The solution B is a formaldehyde (HCHO) (9.5 mL L^{-1}) aqueous solution. The ELD of Ni was performed in a plating bath consisting of a 10:1 (v/v) mixture of solution C and freshly prepared D. The solution C contains nickel (II) sulfate hexahydrate ($Ni_2SO_4 \cdot 6H_2O$) (40 g L^{-1}), sodium citrate (20 g L^{-1}), and lactic acid (10 g L^{-1}) in DI water (pH = 8). The solution D is a dimethylamine borane (1.5 g L^{-1}) aqueous solution.

Fabrication of lithium metal composite yarn: The lithium (Li) metal composite yarn (LMCY) was fabricated via a fast capillary filling of molten Li into the Cu-C yarn at the temperature of 623 K. The fabrication process was conducted in an Ar-filled glove box with

water and oxygen content <0.1 ppm. The fast intake of Li could be fulfilled by simply bringing the edge of Cu-C yarn into contact with molten Li.

Fabrication of yarn-like cathodes: Cathodic materials including lithium iron phosphate (LiFePO$_4$, LFP) or sulfur (S) were mixed with carbon black and polyvinylidene difluoride (PVDF) with a mass ratio of 8:1:1 in N-methyl-2-pyrrolidone (NMP) solvent to form the slurry. The slurry was then coated onto Ni-C yarn via vacuum infiltration. At last, the slurry-coated Ni-C yarn was heated in the vacuum oven to vaporize the NMP solvent, so as to form the yarn-like cathodes. The temperatures for heating LFP and S cathodes were 423 K and 333 K, respectively.

Assembly of wire-type symmetric cells and lithium metal batteries: Wire-type symmetric cells and lithium metal batteries (LMBs) were assembled in an Ar-filled glove box. For the symmetric cells, a pair of LMCYs were sequentially inserted into a polyolefin tube (1 mm in diameter), where they were electrically isolated by a piece of Celgard 2500 separator. Before adding the electrolyte, the cells were partially sealed by heating one end of the polyolefin tube with a heat gun at 373 K. Then, the electrolyte containing 1 M lithium bis(trifluoromethanesulfonyl)imide (LiTFSI) in 1, 3-dioxolane (DOL)/1, 2-dimethoxyethane (DME) with 2 wt% lithium nitrate (LiNO$_3$) was added until it filled the tube. Finally, the tube was heated uniformly, so as to fully seal the battery and remove the excess of the electrolyte. For LMBs, one LMCY and yarn-like cathode were assembled using the same method as the symmetric cell.

Characterizations: The morphologies of Cu-C yarn, LMCY, and yarn-like LFP/S cathodes were characterized by scanning electron microscopy (SEM, TESCAN VEGA3). The material component was confirmed by elemental mapping using an electron probe micro-analyzer (EPMA-1600, Shimadzu, Japan). The crystalline structures of Cu-C yarn and copper oxide-coated C (CuO-C) yarn before and after infusion process were investigated by X-ray diffraction

spectroscopy (XRD) (Bruker D8). The stress-strain curve of LMCY and LMW was obtained using an Instron 5565A tester.

Electrochemical measurements: All the electrochemical performances were tested on the basis of wire-type configuration. The long-term stripping and plating of Li and cycling performances of LMBs were tested with Arbin and Neware battery testing systems. The linear capacity of LMCY was obtained after fully stripping the Li from LMCY at a cut-off voltage of 1 V with Neware battery testing systems. The electrochemical impedance of the full batteries was tested by CHI 660E with a frequency range from 100 kHz to 10 mHz, and a potential amplitude of 5 mV.

Calculation of the ohmic loss of LMCY: To derive the ohmic loss of LMCY from equivalent circuit of wire-type symmetric cell (Figure 3b), we assumed that the electrochemically active sites were uniformly distributed along the LMCY, which resulted in $i_n = i$. The ohmic loss of LMCY (U_{AB}) could be derived from $du = (iL - ix)Rdx$ and $I = iL$, where i is the current density, L is the length of the LMCY, R is the linear resistance of Cu-C yarn.

Calculation of the energy density of wire-type batteries: LMCY or yarn-like cathode possessed a curved ribbon-like geometry with an elliptic section, its volume (V) could be calculated according to the formula: $V = \pi abl/sin\frac{\alpha}{2}$, where a (200 μm) and b (125 μm) are the major semi-axis and minor semi-axis of the elliptical section, respectively, l is the footprint length of the electrode, α (130°) reflects the curvature of the electrode (Figure S2). The weight of LMCY and Ni-C yarn are ~0.6 mg cm^{-1} and ~0.3 mg cm^{-1}, respectively. The mass loading of LFP ranges from 0.25–1.2 mg cm^{-1}. The energy density of the battery can be calculated with the equation: $E = CU/2V$ or $E = CU/M$, where C is the linear capacity, U stands for the discharge voltage of the battery, M is the total weight of cathode, anode, and current collectors.

Simulation study of the infusion process with COMSOL: Multiphysics coupling Two-Phase Flow and Level Set was chosen to mimic the infusion process. The infusion of molten Li into different yarns was essentially a Newtonian fluid that flew in the microfluidic system. Therefore, the inertial force was believed to have a negligible effect on the infusion behavior. The velocity field of molten Li obeyed Stokes equation[49]:$\rho\, \partial \boldsymbol{u}/\partial t = \nabla \cdot \boldsymbol{\sigma}$. In addition, mass conservation required $\partial \rho/\partial t + \nabla \cdot (\rho \boldsymbol{u}) = 0$, giving the incompressibility condition $\nabla \cdot \boldsymbol{u} = 0$ for slow flew of fluids with constant density. In the above equations, ρ denotes the density of molten Li; $\boldsymbol{u}$ is the velocity; $\boldsymbol{\sigma}$ is the stress tensor composed of normal and tangential components, which has been reported elsewhere to be correlated with contact angles [50]. The contact angles of molten Li on the C and Cu were measured as 120° and 30°, respectively. The contact angle of molten Li on the Li_2O was reported as 80°.[38]

Finite element analysis of the mechanical flexibility with ABAQUS: The geometric models of LMCY and LMW were shown in Figure 4d, Q1 and R1. To obtain the same mesh and ensure the fair comparison of flexing stability between LMCY and LMW, both of them possessed the same geometric configuration. That is, 32 twisted fibers with the diameter (D_1) of 10 μm and length (L_1) of 0.5 mm were embedded in a Li cylinder with the diameter (D_2) of 100 μm and length (L_2) of 0.5 mm. The distance between each fiber was $D_3 = 5$ μm. Particularly, those twisted fibers were regarded as Li and Cu-C fibers for LMW and LMCY, respectively. In the modelling, Li was regarded as the elastic-plastic material with work hardening region. The stress-strain (σ-ε) curve of Li under uniaxial tension is described with $\sigma = \begin{cases} E\varepsilon\ (\varepsilon \leq Y/E) \\ K\varepsilon^n\ (\varepsilon > Y/E) \end{cases}$, where E is the elastic modulus, Y is the yield stress (Mises yield criterion), n is the work hardening exponent, and $K = Y(E/Y^n)$. Equal and opposite bending angles ($\beta_1 = 25°, \beta_2 = -25°$) were applied simultaneously on the two ends of LMCY or LMW during the modeling. Besides, a simple element deletion criterion, also known as the tensile failure criterion, was implanted in the above constitutive relation, which can be expressed as $p \geq \sigma_{cut-off}$, where

$p = 1/3 \left(\sigma_x + \sigma_y + \sigma_z \right)$ is the hydrostatic pressure, $\sigma_{cut-off}$ is the user defined cut-off pressure (the maximum tensile stress of Li before crack). The material properties and the boundary conditions of the simulation were listed in Table S2.

Supporting Information

Supporting Information is available from the Wiley Online Library or from the author.

Conflict of Interest

The authors declare no conflict interest.

References

[1]   W. Gao, S. Emaminejad, H. Y. Y. Nyein, S. Challa, K. Chen, A. Peck, H. M. Fahad, H. Ota, H. Shiraki, D. Kiriya, *Nature* **2016**, *529*, 509.

[2]   M. Hamedi, R. Forchheimer, O. Inganäs, *Nat. Mater.* **2007**, *6*, 357–362.

[3]   A. Maziz, A. Concas, A. Khaldi, J. Stålhand, N.-K. Persson, E. W. Jager, *Sci. Adv.* **2017**, *3*, e1600327.

[4]   Y. Wu, S. S. Mechael, C. Lerma, R. S. Carmichael, T. B. Carmichael, *Matter* **2020**, *2*, 882–895.

[5]   P.-C. Hsu, A. Y. Song, P. B. Catrysse, C. Liu, Y. Peng, J. Xie, S. Fan, Y. Cui, *Science* **2016**, *353*, 1019–1023.

[6]   X. Pu, L. Li, H. Song, C. Du, Z. Zhao, C. Jiang, G. Cao, W. Hu, Z. L. Wang, *Adv. Mater.* **2015**, *27*, 2472–2478.

[7]   X. Shi, Y. Zuo, P. Zhai, J. Shen, Y. Yang, Z. Gao, M. Liao, J. Wu, J. Wang, X. Xu, *Nature* **2021**, *591*, 240–245.

[8]   I. Wicaksono, C. I. Tucker, T. Sun, C. A. Guerrero, C. Liu, W. M. Woo, E. J. Pence, C. Dagdeviren, *npj Flex. Electron.* **2020**, *4*, 1–13.

[9]   M. Tebyetekerwa, I. Marriam, Z. Xu, S. Yang, H. Zhang, F. Zabihi, R. Jose, S. Peng, M. Zhu, S. Ramakrishna, *Energy Environ. Sci.* **2019**, *12*, 2148–2160.

[10]   A. Bandodkar, S. Lee, I. Huang, W. Li, S. Wang, C.-J. Su, W. Jeang, T. Hang, S. Mehta, N. Nyberg, *Nat. Electron.* **2020**, *3*, 554–562.

[11]   Y. Gao, C. Xie, Z. Zheng, *Adv. Energy Mater.* **2021**, *11*, 2002838.

[12]   A. M. Zamarayeva, A. E. Ostfeld, M. Wang, J. K. Duey, I. Deckman, B. P. Lechêne, G. Davies, D. A. Steingart, A. C. Arias, *Sci. Adv.* **2017**, *3*, e1602051.

[13]   J. Ren, Y. Zhang, W. Bai, X. Chen, Z. Zhang, X. Fang, W. Weng, Y. Wang, H. Peng, *Angew. Chem. Int. Edit.* **2014**, *53*, 7864–7869.

[14]   Y. Xu, Y. Zhang, Z. Guo, J. Ren, Y. Wang, H. Peng, *Angew. Chem. Int. Edit.* **2015**, *54*, 15390–15394.

[15]   Y. H. Kwon, S. W. Woo, H. R. Jung, H. K. Yu, K. Kim, B. H. Oh, S. Ahn, S. Y. Lee, S. W. Song, J. Cho, *Adv. Mater.* **2012**, *24*, 5192–5197.

[16]   Y. Zhou, C. H. Wang, W. Lu, L. Dai, *Adv. Mater.* **2020**, *32*, 1902779.

[17]   Q. Wang, H. Yang, T. Meng, J. Yang, B. Huang, F. L. Gu, S. Zhang, C. Meng, Y. Tong, *Energy Stor. Mater.* **2021**, *36*, 365-375.

[18]   T. Meng, B. Li, Q. Wang, J. Hao, B. Huang, F. L. Gu, H. Xu, P. Liu, Y. Tong, *ACS Nano* **2020**, *14*, 7066-7076.

[19]   Q. Wang, T. Meng, Y. Li, J. Yang, B. Huang, S. Ou, C. Meng, S. Zhang, Y. Tong, *Energy Stor. Mater.* **2021**, *39*, 354-364.

[20] W. Xu, J. Wang, F. Ding, X. Chen, E. Nasybulin, Y. Zhang, J.-G. Zhang, *Energy Environ. Sci.* **2014**, *7*, 513–537.

[21] W. G. Chong, J. Q. Huang, Z. L. Xu, X. Qin, X. Wang, J. K. Kim, *Adv. Funct. Mater.* **2017**, *27*, 1604815.

[22] Y. Zhang, L. Wang, Z. Guo, Y. Xu, Y. Wang, H. Peng, *Angew. Chem. Int. Edit.* **2016**, *55*, 4487–4491.

[23] T. Liu, Q. C. Liu, J. J. Xu, X. B. Zhang, *Small* **2016**, *12*, 3101–3105.

[24] J. Zhou, X. Li, C. Yang, Y. Li, K. Guo, J. Cheng, D. Yuan, C. Song, J. Lu, B. Wang, *Adv. Mater.* **2019**, *31*, 1804439.

[25] A. Wang, S. Tang, D. Kong, S. Liu, K. Chiou, L. Zhi, J. Huang, Y. Y. Xia, J. Luo, *Adv. Mater.* **2018**, *30*, 1703891.

[26] A. Masias, N. Felten, R. Garcia-Mendez, J. Wolfenstine, J. Sakamoto, *J. Mater. Sci.* **2019**, *54*, 2585–2600.

[27] B. Yu, T. Tao, S. Mateti, S. Lu, Y. Chen, *Adv. Funct. Mater.* **2018**, *28*, 1803023.

[28] Y. Liu, D. Lin, Z. Liang, J. Zhao, K. Yan, Y. Cui, *Nat. Commun.* **2016**, *7*, 10992.

[29] D. Lin, Y. Liu, Z. Liang, H.-W. Lee, J. Sun, H. Wang, K. Yan, J. Xie, Y. Cui, *Nat. Nanotechnol.* **2016**, *11*, 626.

[30] R. Zhang, X. Chen, X. Shen, X.-Q. Zhang, X.-R. Chen, X.-B. Cheng, C. Yan, C.-Z. Zhao, Q. Zhang, *Joule* **2018**, *2*, 764-777.

[31] X. Wang, Z. Pan, J. Yang, Z. Lyu, Y. Zhong, G. Zhou, Y. Qiu, Y. Zhang, J. Wang, W. Li, *Energy Stor. Mater.* **2019**, *22*, 179–184.

[32] J. Wang, H. Wang, J. Xie, A. Yang, A. Pei, C.-L. Wu, F. Shi, Y. Liu, D. Lin, Y. Gong, *Energy Stor. Mater.* **2018**, *14*, 345–350.

[33] E. Saiz, R. Cannon, A. Tomsia, *Acta. Mater.* **2000**, *48*, 4449–4462.

[34] O. Dezellus, N. Eustathopoulos, *J. Mater. Sci.* **2010**, *45*, 4256-4264.

[35]   X. Liu, H. Chang, Y. Li, W. T. Huck, Z. Zheng, *ACS Appl. Mater. Interfaces* **2010**, *2*, 529–535.

[36]   P. Li, Y. Zhang, Z. Zheng, *Adv. Mater.* **2019**, *31*, 1902987.

[37]   X.-Y. Yue, W.-W. Wang, Q.-C. Wang, J.-K. Meng, Z.-Q. Zhang, X.-J. Wu, X.-Q. Yang, Y.-N. Zhou, *Energy Stor. Mater.* **2018**, *14*, 335–344.

[38]   S. Krat, A. Popkov, Y. M. Gasparyan, A. Pisarev, P. Fiflis, M. Szott, M. Christenson, K. Kalathiparambil, D. N. Ruzic, *Fusion Eng. Des.* **2017**, *117*, 199–203.

[39]   H. Tian, J. Shao, Y. Ding, X. Li, H. Liu, *Langmuir* **2013**, *29*, 4703–4714.

[40]   T. Hoshide, Y. Zheng, J. Hou, Z. Wang, Q. Li, Z. Zhao, R. Ma, T. Sasaki, F. Geng, *Nano Lett.* **2017**, *17*, 3543–3549.

[41]   F. Mo, G. Liang, Z. Huang, H. Li, D. Wang, C. Zhi, *Adv. Mater.* **2020**, *32*, 1902151.

[42]   P. Bai, J. Li, F. R. Brushett, M. Z. Bazant, *Energy Environ. Sci.* **2016**, *9*, 3221–3229.

[43]   R. Liu, Y. Liu, J. Chen, Q. Kang, L. Wang, W. Zhou, Z. Huang, X. Lin, Y. Li, P. Li, *Nano Energy* **2017**, *33*, 325–333.

[44]   C. Song, Y. Li, H. Li, T. He, Q. Guan, J. Yang, X. Li, J. Cheng, B. Wang, *Nano Energy* **2019**, *60*, 285–293.

[45]   Z. Guo, Y. Zhao, Y. Ding, X. Dong, L. Chen, J. Cao, C. Wang, Y. Xia, H. Peng, Y. Wang, *Chem* **2017**, *3*, 348–362.

[46]   Y. Li, C. Zhong, J. Liu, X. Zeng, S. Qu, X. Han, Y. Deng, W. Hu, J. Lu, *Adv. Mater.* **2018**, *30*, 1703657.

[47]   Z. Liu, K. Chen, A. Fernando, Y. Gao, G. Li, L. Jin, H. Zhai, Y. Yi, L. Xu, Y. Zheng, *Chem. Eng. J.* **2020**, *403*, 126191.

[48]   Y. Gao, Q. Guo, Q. Zhang, Y. Cui, Z. Zheng, *Adv. Energy Mater.* **2020**, 2002580.

[49]   T. M. Squires, S. R. Quake, *Rev. Mod. Phys.* **2005**, *77*, 977.

[50]   H. Tian, J. Shao, H. Hu, L. Wang, Y. Ding, *ACS Appl. Mater. Interfaces* **2016**, *8*, 16419–16427.

[51]   H. Li, Z. Liu, G. Liang, Y. Huang, Y. Huang, M. Zhu, Z. Pei, Q. Xue, Z. Tang, Y. Wang, *ACS Nano* **2018**, *12*, 3140-3148.

[52]   N. Zhang, F. Huang, S. Zhao, X. Lv, Y. Zhou, S. Xiang, S. Xu, Y. Li, G. Chen, C. Tao, *Matter* **2020**, *2*, 1260–1269.
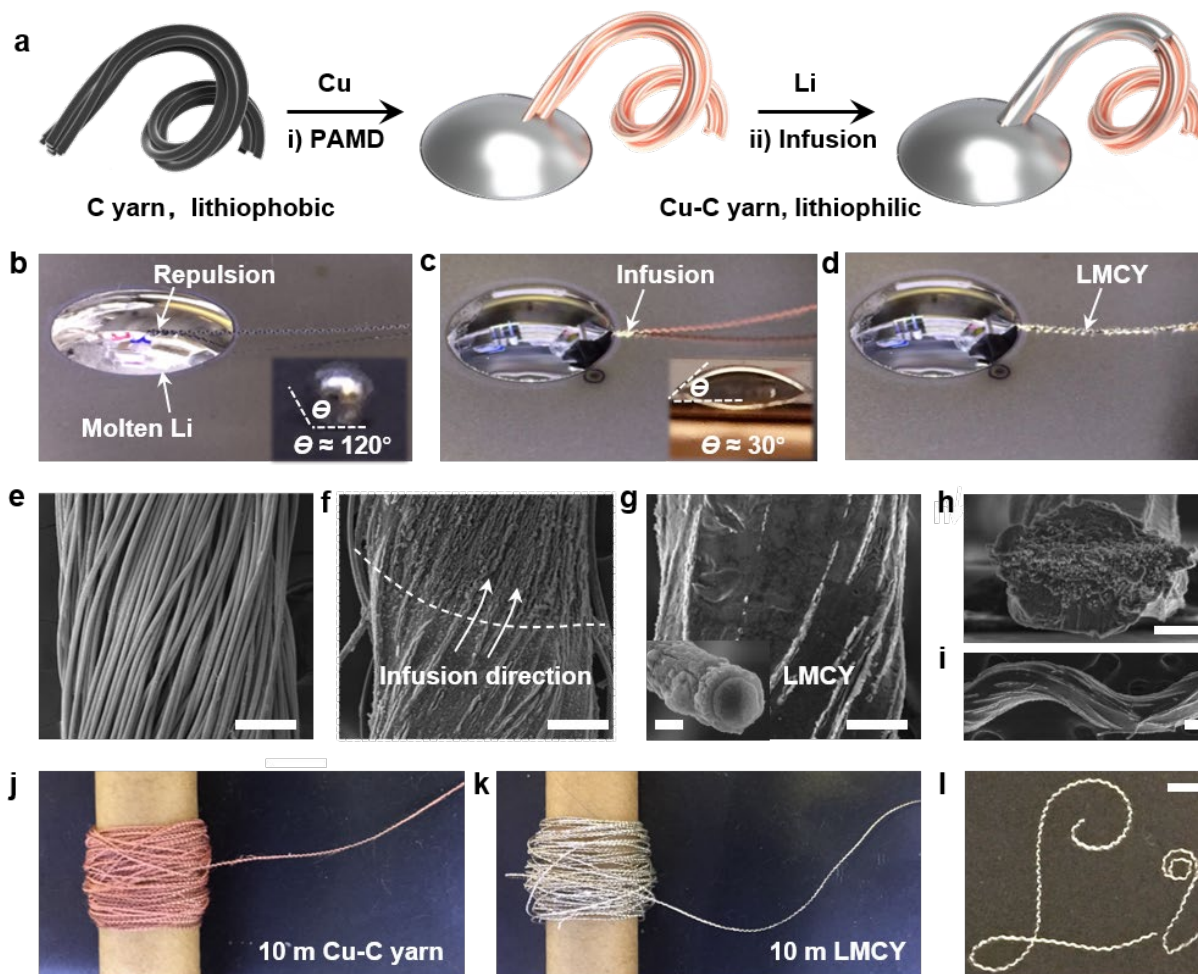
Figure 1. Fabrication and characterizations of lithium metal composite yarn (LMCY). a) Schematic illustration of the fabrication of LMCY. The process includes i) conformal deposition of lithiophilic copper (Cu) onto carbon (C) yarn via polymer-assisted metal deposition (PAMD); ii) capillary filling of molten lithium (Li) into the Cu-coated C (Cu-C) yarn. b) Optical image of the C yarn after being put into the molten Li. Inset shows the contact angle of the molten Li on the graphite at 623 K. c, d) Optical images of the infusion of molten Li into the Cu-C yarn. Inset shows the contact angle of the molten Li on the Cu at 623 K. e) Morphology of Cu-C yarn. f) Morphological change of Cu-C yarn during the infusion process. The white dash line marks the boundary between Li-filled (below part) and non-filled (up part) Cu-C yarn. The white arrows point the infusion direction. g–i) Morphologies of LMCY. Inset shows a single Li-coated Cu-C fiber. j, k) A scroll of ten-meter-long Cu-C yarn and LMCY,

respectively. l) A chemical symbol of "Li" made with flexible LMCY. The symbol has a minimum bending radius of 1 mm. Scale bars: e–i): 100 μm, inset, 5 μm; l): 4 mm.
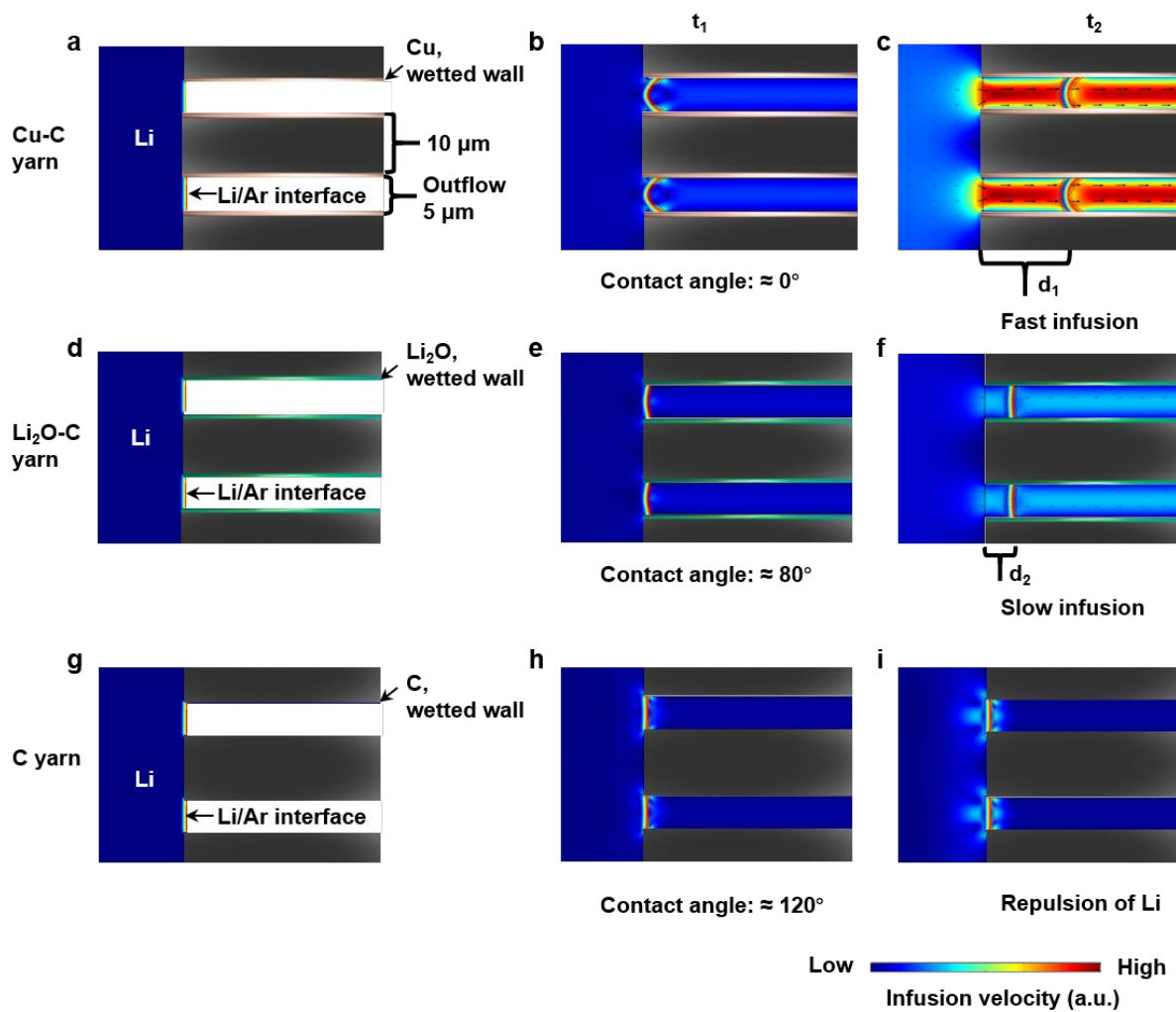
Figure 2. Simulation study of the infusion process. a, d, g) Geometric models of Cu-C yarn, lithium oxide-coated C (Li$_2$O-C) yarn, and C yarn that immersed in the molten Li, respectively. b, e, h) Morphologies of the interface between molten Li and argon (Ar) at t_1. c, f, i) Morphologies of the interface between molten Li and Ar at t_2. d_1 and d_2 show the infusion lengths of the molten Li in the Cu-C yarn and Li$_2$O-C, respectively.
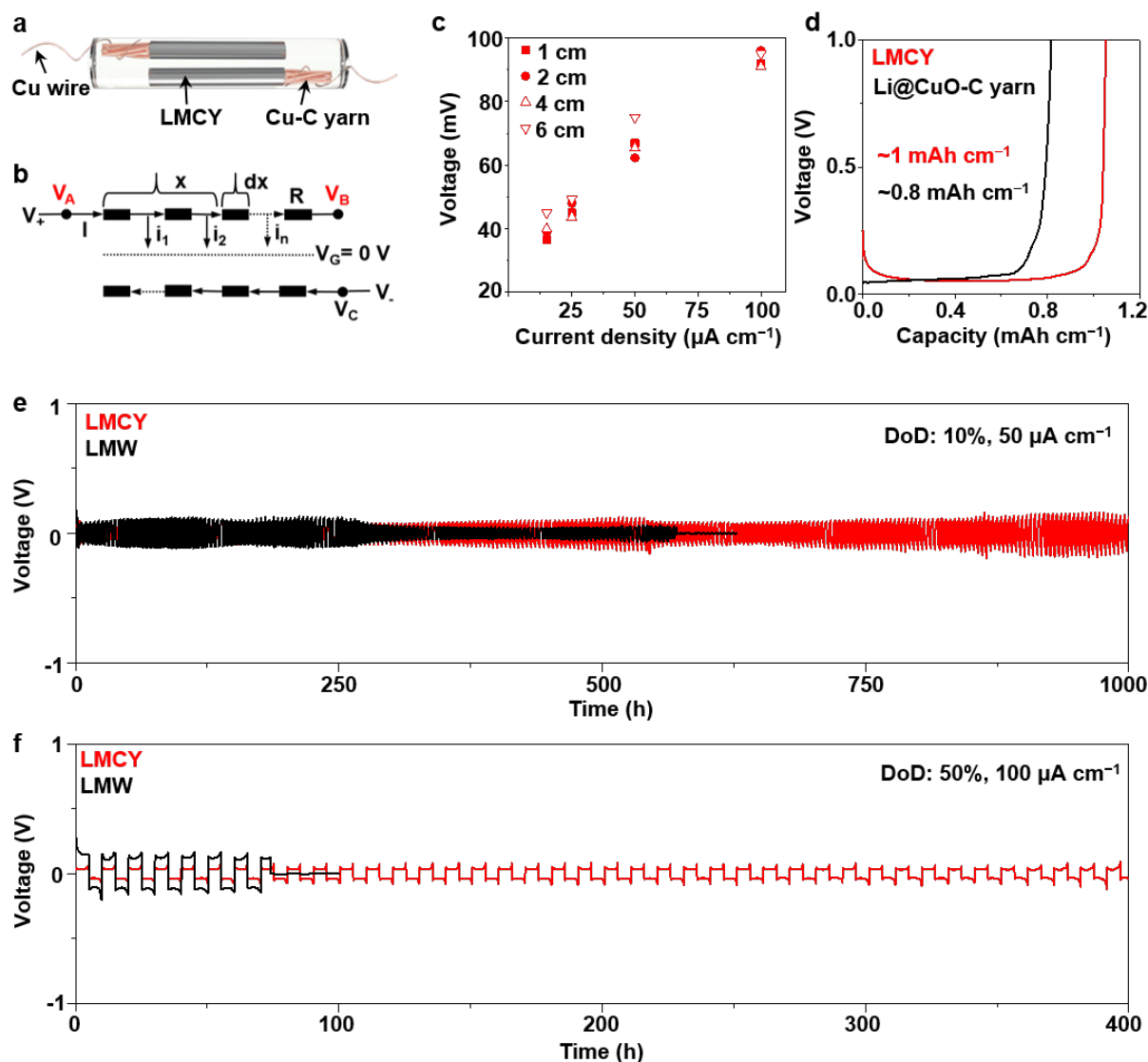
Figure 3. Electrochemical performances of LMCY. a) Schematic image of the wire-type symmetric cell using a pair of LMCYs. b) Equivalent circuit of the symmetric cell. c) Overpotentials of symmetric cells at different lengths, recorded at different current densities. d) The linear capacities of LMCY and the Li yarn using CuO-C as the host, respectively. e) Cycling performances of symmetric cells using a pair of LMCYs or LMWs, recorded at DoD: 10%, 50 μA cm^{-1}. f) Cycling performances of symmetric cells using a pair of LMCYs or LMWs, recorded at DoD: 50%, 100 μA cm^{-1}.
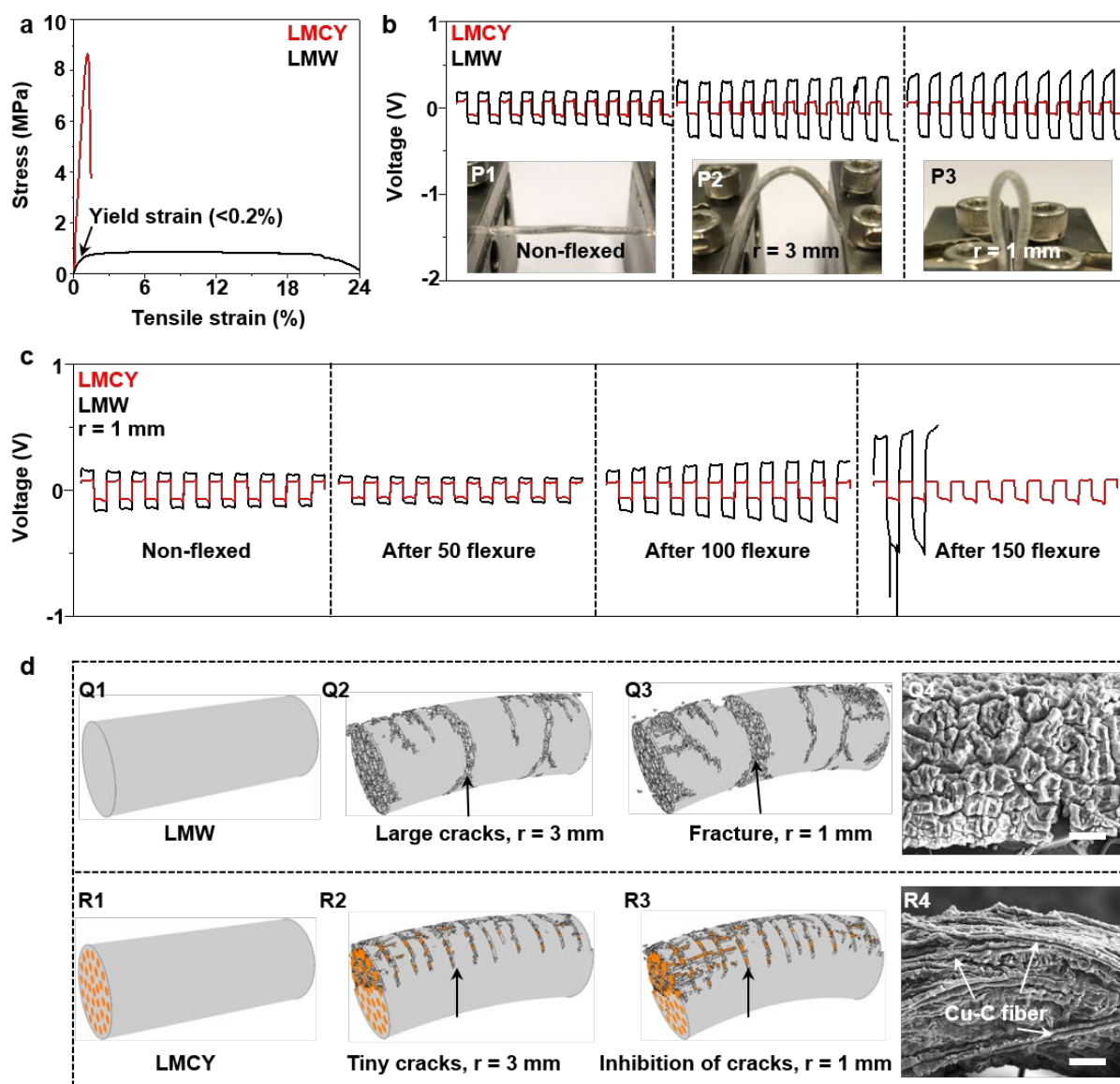
Figure 4. Flexibility of LMCY. a) Tensile stress-strain curve of LMCY and LMW. b) Overpotentials of wire-type symmetric cells using a pair of LMCYs or LMWs, recorded at non-flexed condition (P1), flexing at a radius of 3 mm (P2), and flexing at a radius of 1 mm (P3). c) Mechanical durability of both types of symmetric cells, tested at a DoD and a current density of 10% and 100 µA cm^{-1}, respectively. The cells were subjected to multiple flexures at a flexing radius of 1 mm, then tested at a non-flexed status. d) Finite element (FE) analysis on the crack behaviors of LMW (Q1) and LMCY (R1) at the flexing radii of 3 mm (Q2 and R2) and 1 mm (Q3 and R3). Q4 and R4 show the sectional images of LMW and LMCY after repeated flexed at a radius of 1 mm. The grey and yellow colors represent Li and Cu-C fiber, respectively. The

diameter of Cu-C fiber is 10 μm; the distance between neighboring fiber is 5 μm. Scale bars:

Q4, R4: 50 μm
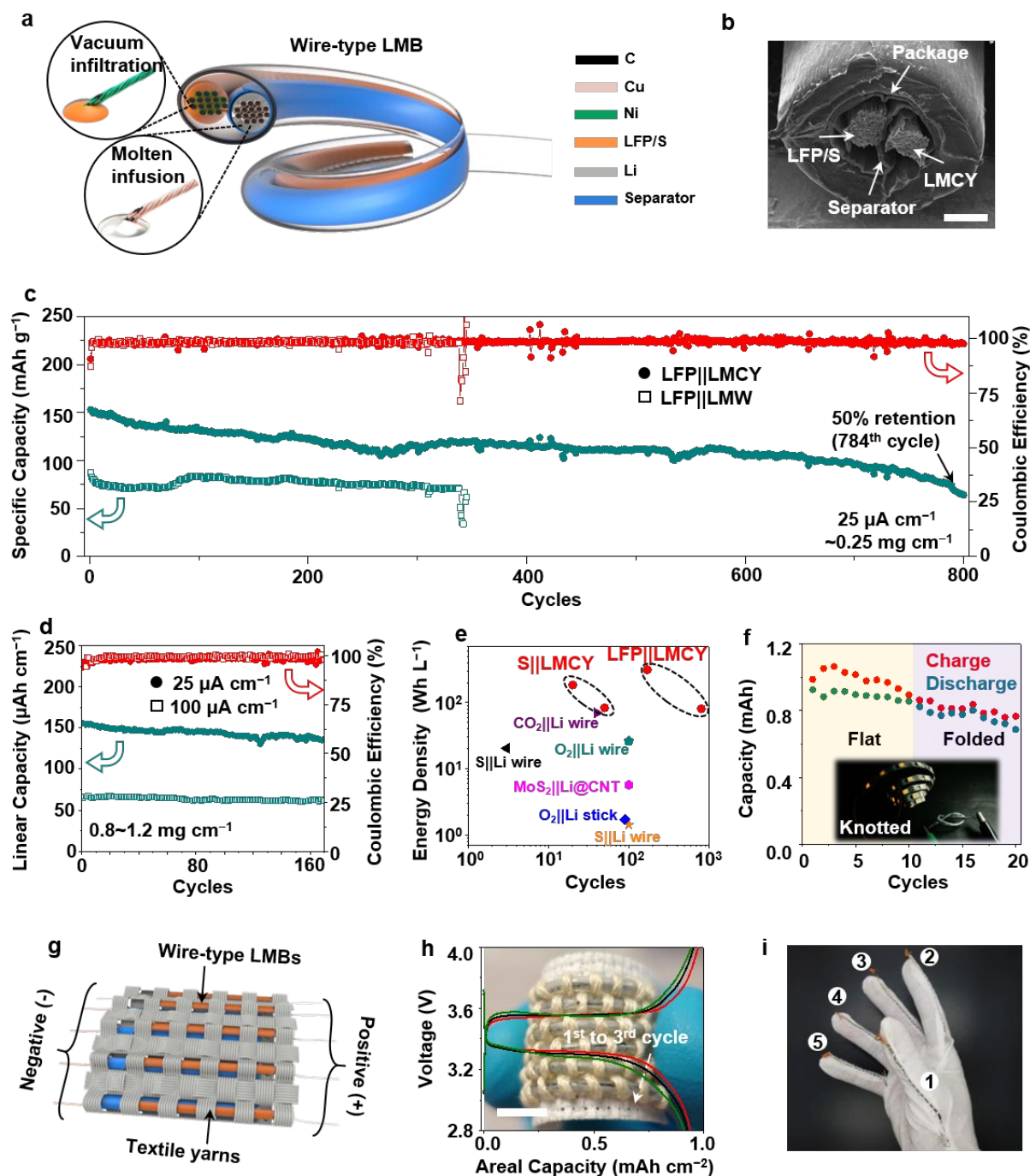
Figure 5. Characterization and electrochemical performances of wire-type lithium metal batteries (LMBs). a) Schematic image of the wire-type LMB. b) Sectional SEM image of as-fabricated wire-type LMB. c) Cycling performances of LFP||LMCY and LFP||LMW, recorded at 25 µA cm^{-1} (~0.5 C). d) Cycling performances of LFP||LMCY with a high mass loading of LFP (0.8~1.2 mg cm^{-1}). e) Performances benchmark with state-of-the-art wire-type LMBs. f) Foldability test of the LFP||LMCY. Inset shows the optical image of a knotted LFP||LMCY that

powered 36 LED arrays. g) Schematic image of the battery textile. h) Voltage profiles of the battery textile. Inset shows the optical image of as-fabricated battery textile. i) Optical image of as-fabricated battery glove. The battery glove consists of five LFP‖LMCY that embedded along the seam line of each battery finger. Scale bar: b) 200 μm; h) 0.5 cm

Table 1. Performance metrics of our wire-type lithium metal batteries (LMBs).

Cathode	Mass loading (mg cm^{-1})	Cycles	Retention (%)	Current density (μA cm^{-1})	Linear capacity (μAh cm^{-1})	Energy density (Wh L^{-1})
LFP	~0.25	800	42	25 (~0.5 C)	37.3	70.5
LFP	~0.5	400	34	100	50.3	90.5
LFP	~1.2	170	88	25 (~0.15 C)	150.9	292.4
LFP	~0.8	170	92	100	68.3	122.4

Table of Content

Yuan Gao, Hong Hu, Jian Chang, Qiyao Huang, Qiuna Zhuang, Peng Li, and Zijian Zheng*

Realizing High-Energy and Stable Wire-Type Batteries with Flexible Lithium Metal Composite Yarns
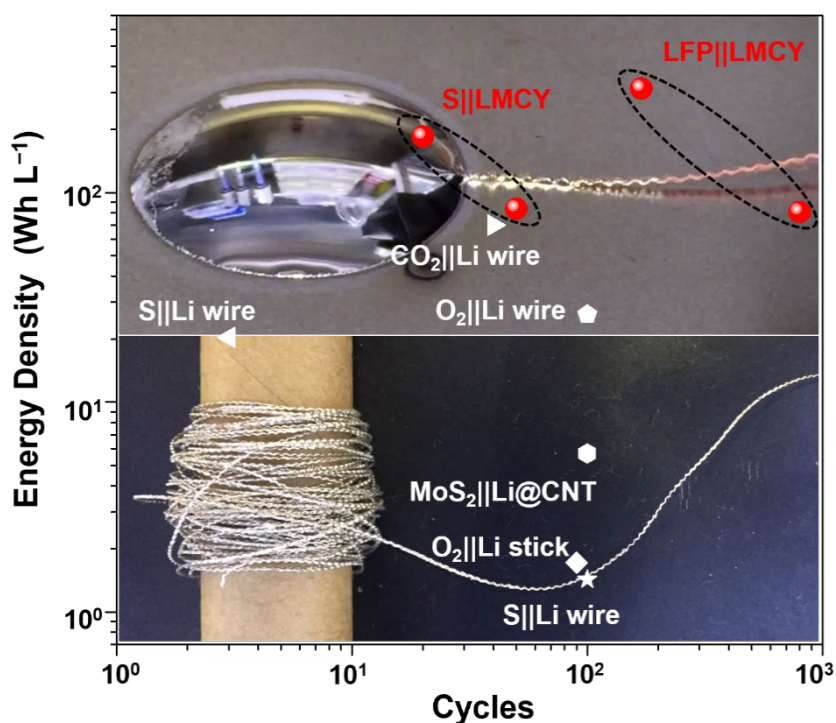
High-capacity, stable, and flexible lithium metal composite yarns (LMCYs) are realized via the fast and scalable capillary filling, a non-reactive wetting process without the use of lithium-reactive materials. The use of LMCYs as anodes endows wire-type lithium metal batteries (LMBs) with a high energy density of ~293 Wh L^{-1}, a long cyclic life over 800 cycles, and good foldability.

Realizing High-Energy and Stable Wire-Type Batteries with Flexible Lithium Metal Composite Yarns

Yuan Gao, Hong Hu, Jian Chang, Qiyao Huang, Qiuna Zhuang, Peng Li, and Zijian Zheng*
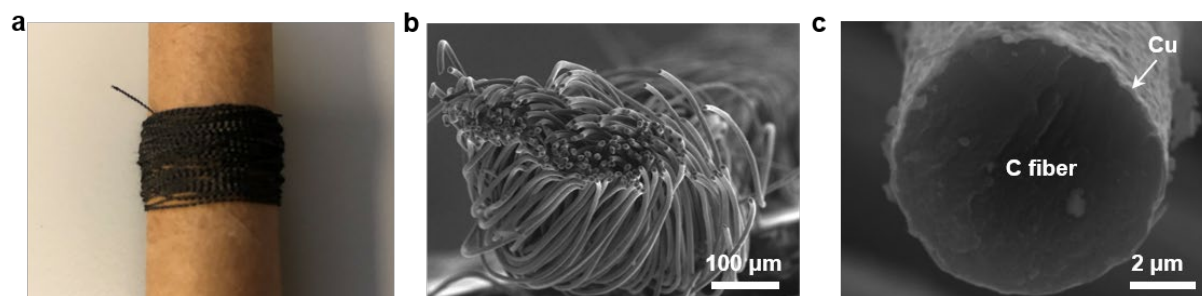
Figure S1. Characterization of carbon (C) yarn and copper (Cu)-coated C (Cu-C) yarn. a, b) Optical and scanning electron microscopy (SEM) images of the pristine C yarn. The C yarn consists of 200 twisted C fibers. c) SEM image of Cu-C fiber. Highly conductive Cu (~200 nm) can be uniformly coated onto each C fiber via the method of PAMD.
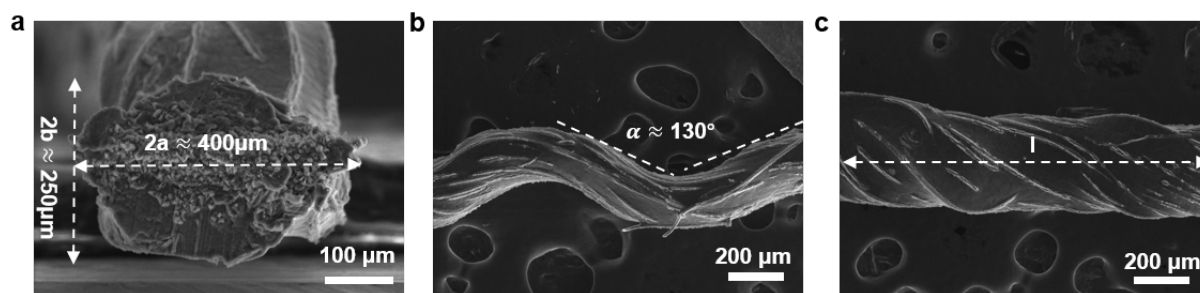
Figure S2. The geometry of lithium metal composite yarn (LMCY).
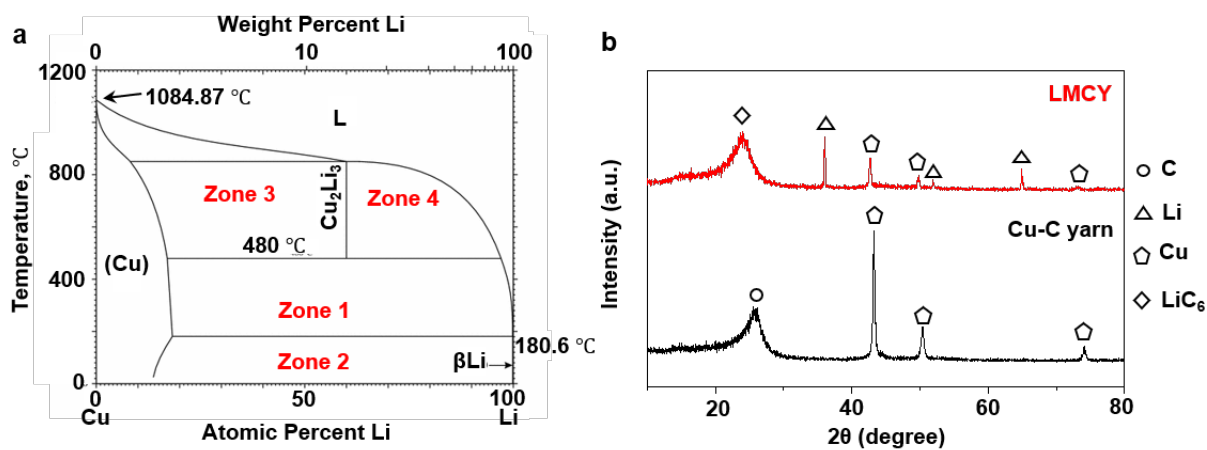
Figure S3. Characterization of Cu-C yarn and LMCY. a) Phase diagram of Cu-lithium (Li). The infusion of molten Li into Cu-C yarn is performed at the temperature of 350 ℃ (Zone 1), no intermetallic bonds are thus formed between Cu and Li. b) X-ray diffraction spectroscopy (XRD) of Cu-C yarn and LMCY.
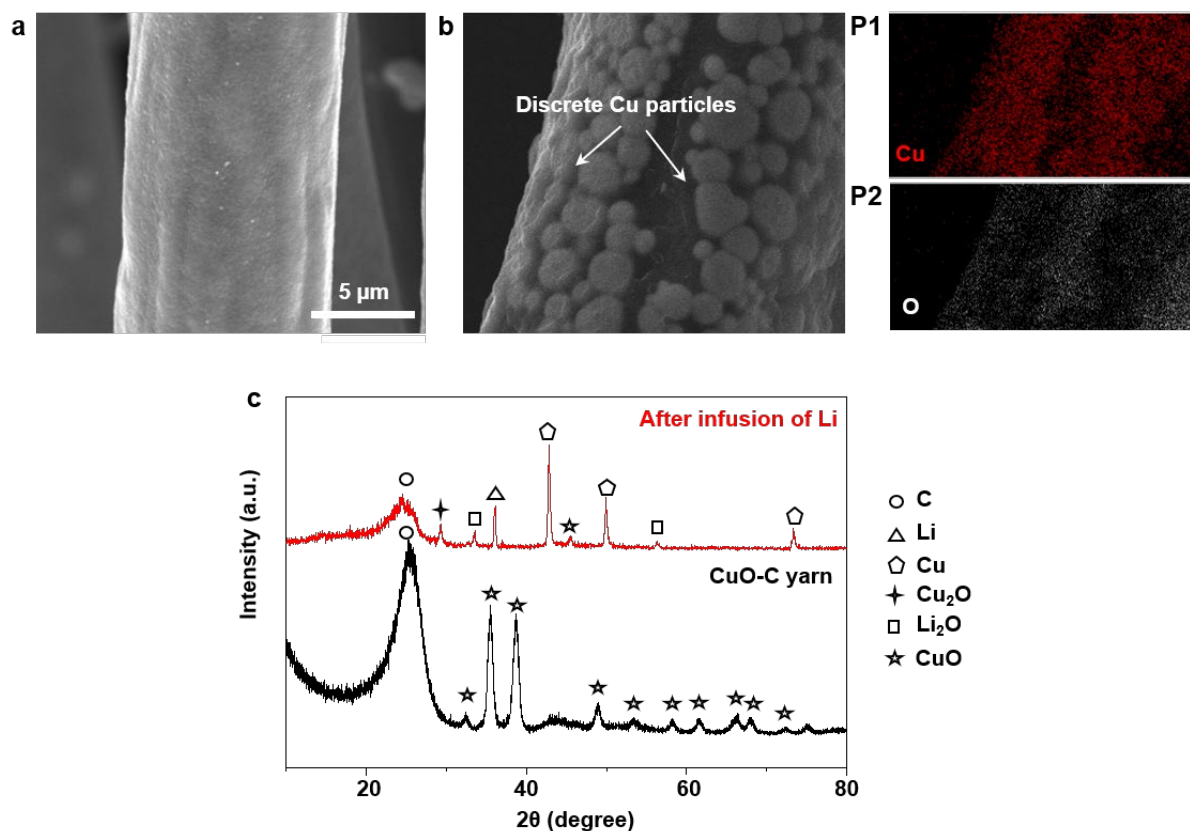
Figure S4. Characterization of copper oxide (CuO)-C yarn before and after infusion of molten Li. a) Morphology of a CuO-C fiber. b) Morphology of a CuO-C fiber after reaction with molten Li. The reaction between CuO and molten Li reduces the dense CuO film into discrete Cu particles and generates a large amount of lithium oxide (Li_2O). Energy-dispersive X-ray spectroscopy (EDX) shows the distribution of Cu (P1) and oxygen (O) (P2), of which O should come from Li_2O. Li can not be detected by EDX. The Li_2O forms a new interface between molten Li and the substrate, which hinders the infusion of molten Li into the host. c) XRD of CuO-C yarn before and after infusion of molten Li. The peaks at 42.8 °, 50 ° and 73.3 ° indicate the formation of Cu, resulting from the chemical reduction of CuO by molten Li.
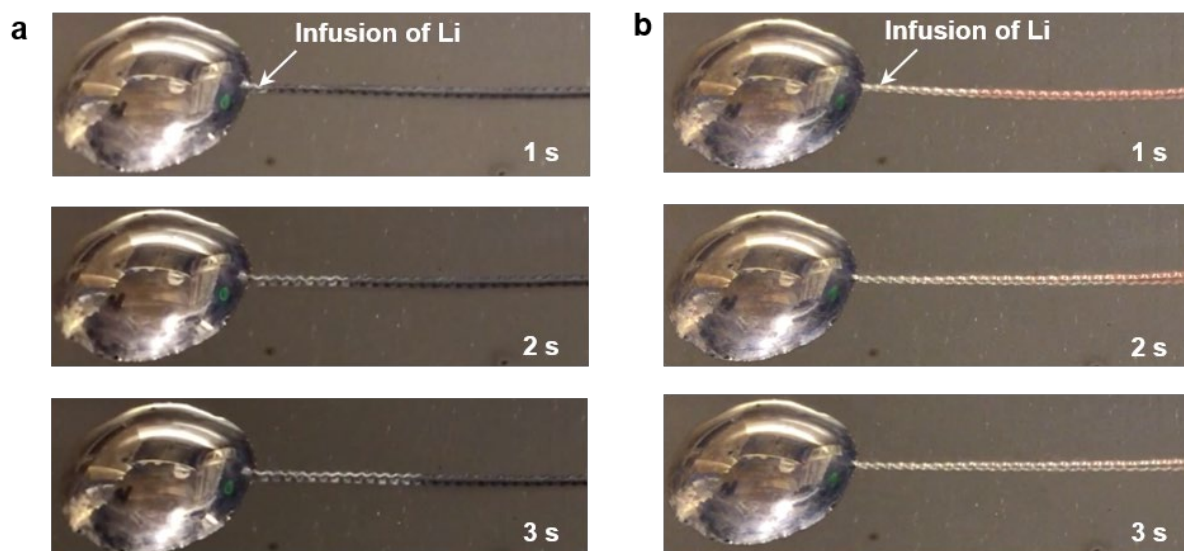
Figure S5. Optical images of the infusion of molten Li into different hosts. a) Infusion of molten Li into CuO-C yarn. b) Infusion of molten Li into Cu-C yarn. The length of the yarn is 4 cm. The black and red colors are the CuO-C yarn and Cu-C yarn, respectively. The white color shows the infused Li. The average infusion velocities are 70 cm min^{-1} and 32 cm min^{-1} for Cu-C yarn and CuO-C yarn, respectively.
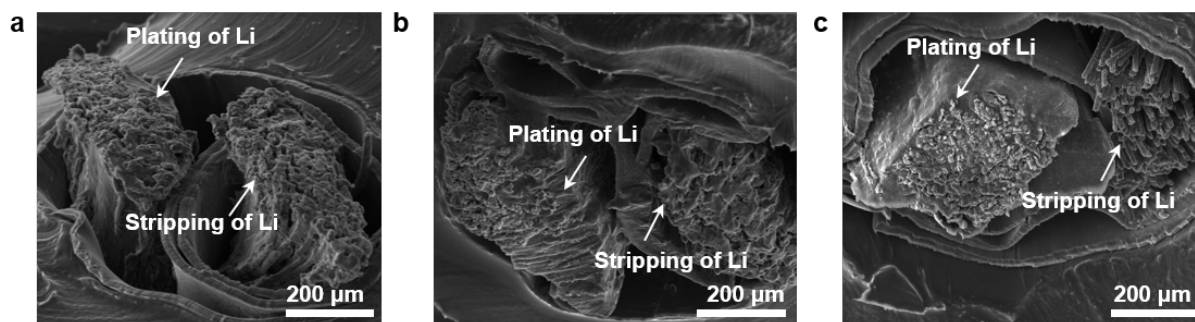
Figure S6. SEM images of LMCYs during stripping and plating of Li. a) Stripping and plating of Li at 0.25 mAh cm^{-1}. b) Stripping and plating of Li at 0.5 mAh cm^{-1}. c) Stripping and plating of Li at 1 mAh cm^{-1}.

a

b

c

d
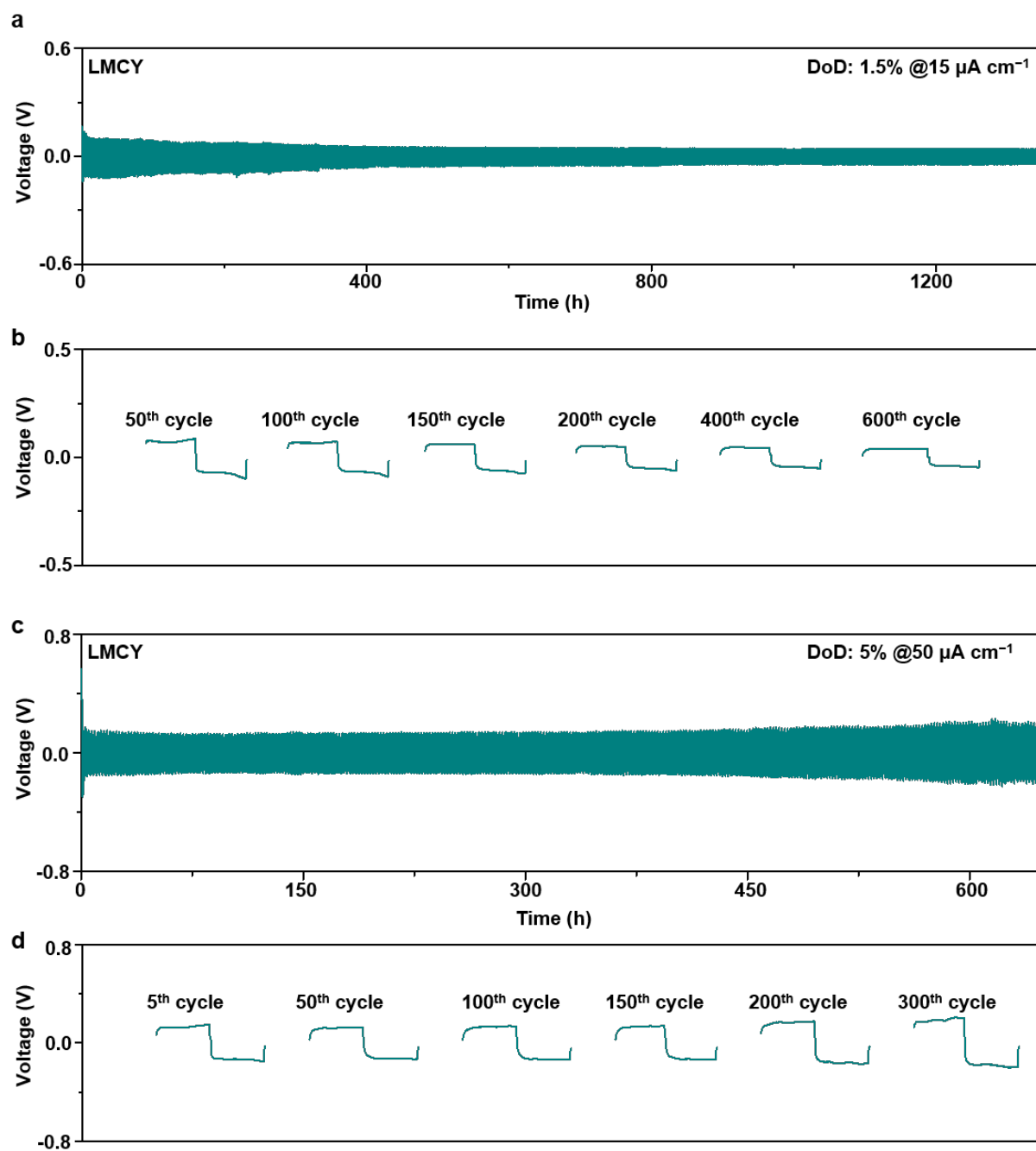
Figure S7. Long-term stripping and plating of Li. a, b) Cycling performance and overpotentials of LMCY at a DoD of 1.5% and a current density of 15 μA cm^{-1}. c, d) Cycling performance and overpotentials of LMCY at a DoD of 5% and a current density of 50 μA cm^{-1}.

40

a

LMCY

DoD: 25% @100 µA cm^{-1}

Voltage (V)

0.5

0.0

-0.5

Time (h)

0   80   160   240   320   400

b

LMCY

DoD: 60% @100 µA cm^{-1}

Voltage (V)

0.8

0.0

-0.8

Time (h)

0   60   120   180   240
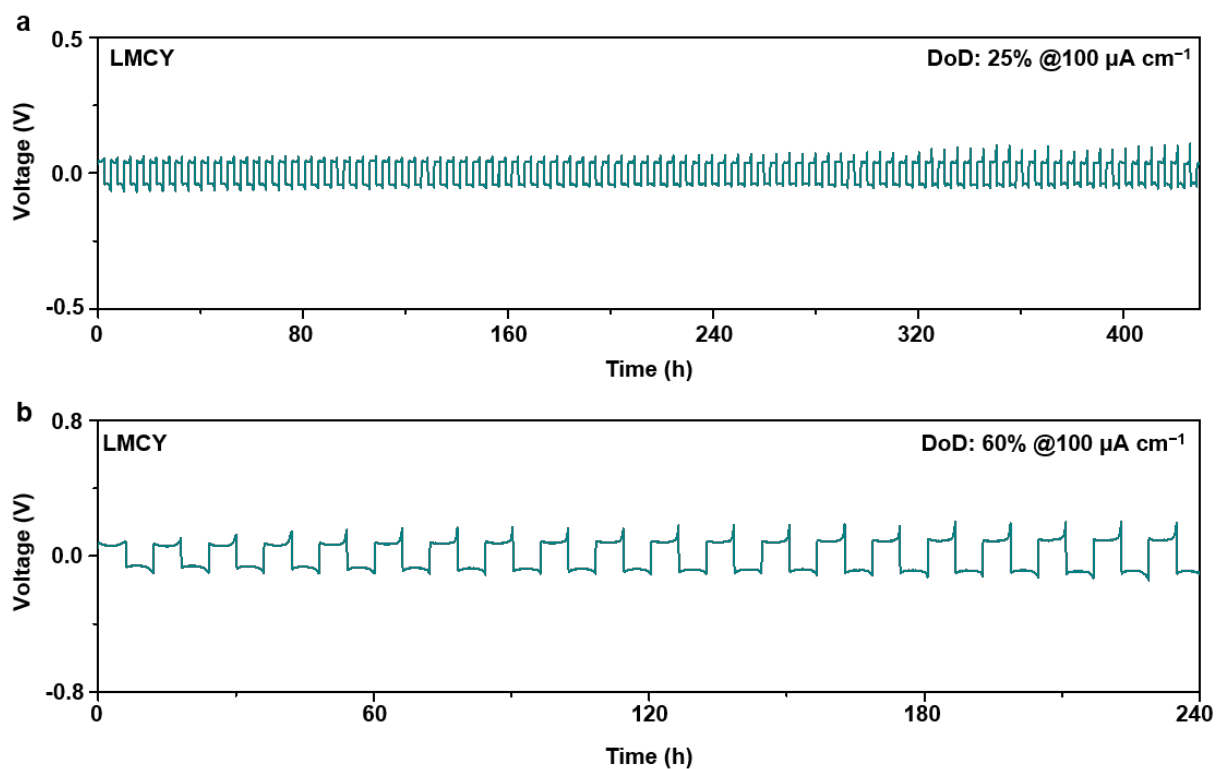
Figure S8. Long-term stripping and plating of Li at a high current density of 100 µA cm^{-1}. a) Cycling performance of LMCY at a DoD of 25%. b) Cycling performance of LMCY at a DoD of 60%.
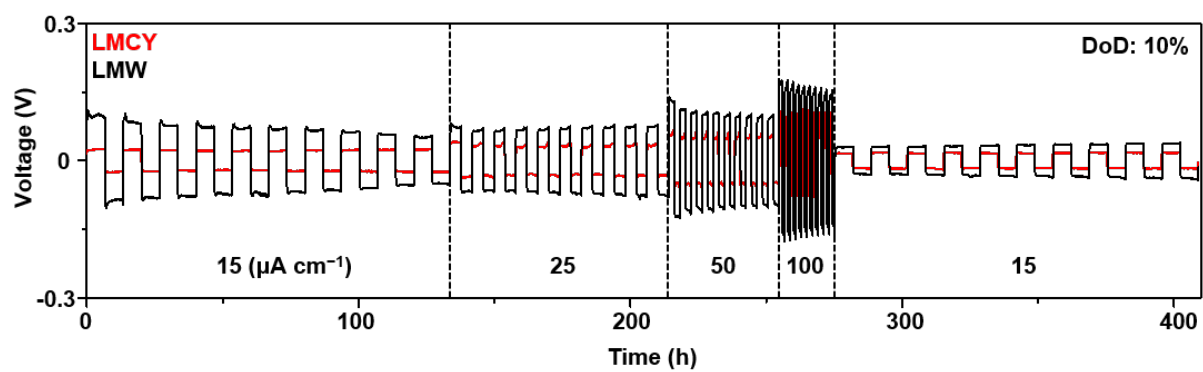
Figure S9. Rate performance of wire-type symmetric cells using a pair of LMCYs or lithium metal wires (LMW)s.
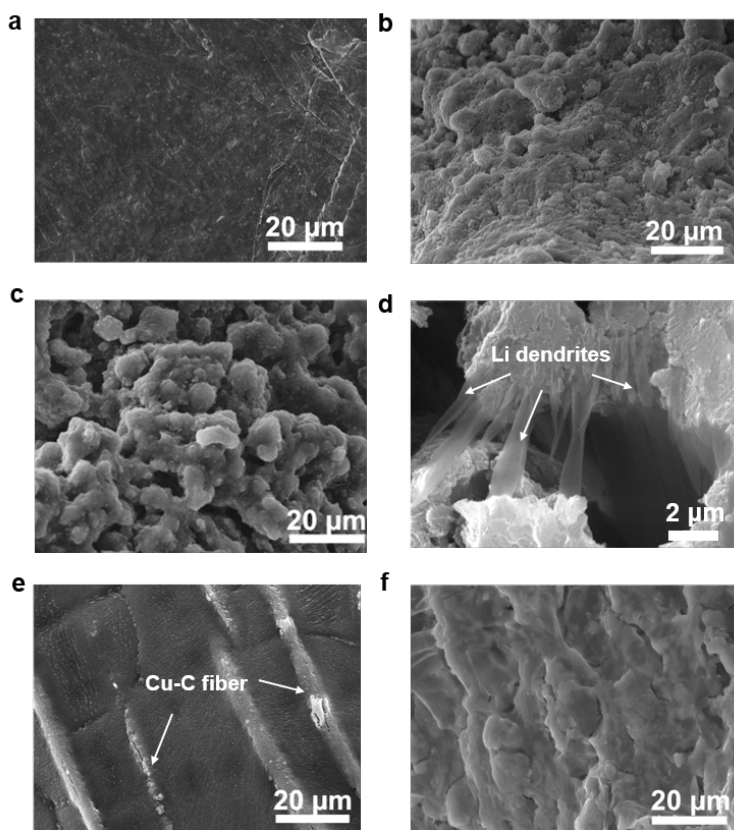
Figure S10. SEM images of LMCYs and LMWs before and after long-term stripping and plating of Li. a, b) LMCYs and LMWs before cyclic test. c, d) LMWs after cyclic test for 400 hrs and 600 hrs at a current density and DoD of 50 µA cm^{-1} and 10%. e) LMWs after cyclic test for 80 hrs at a current density and DoD of 100 µA cm^{-1} and 50%. The formation of Li dendrites caused the short circuit of the cell. f) LMCYs after cyclic test for 400 hrs at a current density and DoD of 100 µA cm^{-1} and 50%. LMCYs still showed a quasi-smooth surface.
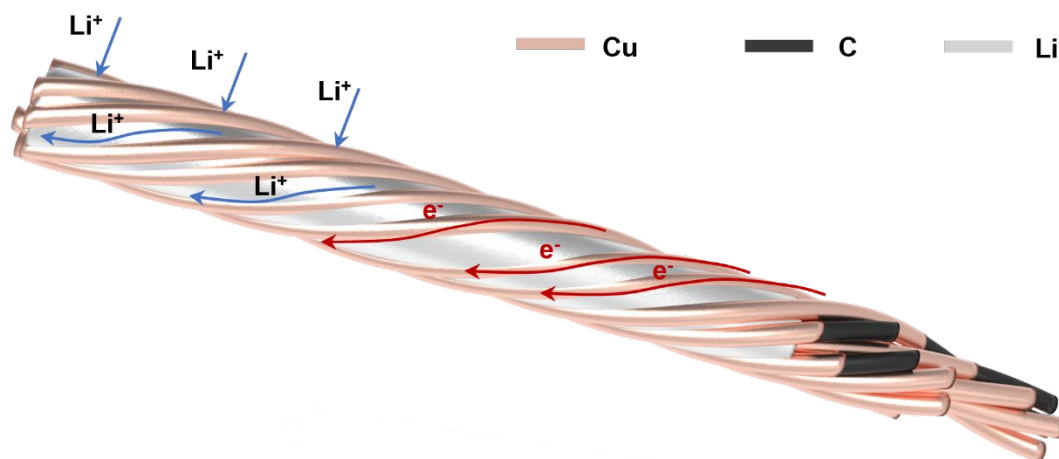
a. High electrical conductivity of Cu-C yarn for the fast electron transport.

b. Porous structure of Cu-C yarn for the unrestricted diffusion of electrolyte ions and the accommodation of Li deposition.

c. Large surface area of Cu-C yarn for the reduction of the localized current density and stabilization of SEI.

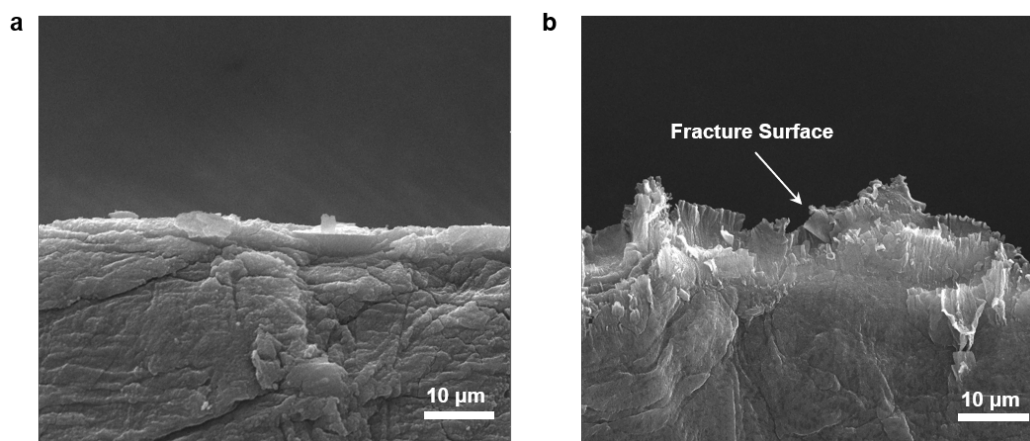**Figure S11.** Schematic image of the advantages of Cu-C yarn.

Figure S12. Morphologies of LMWs before and after bending test. LMW underwent plastic deformation and fracture after repeatedly bent.
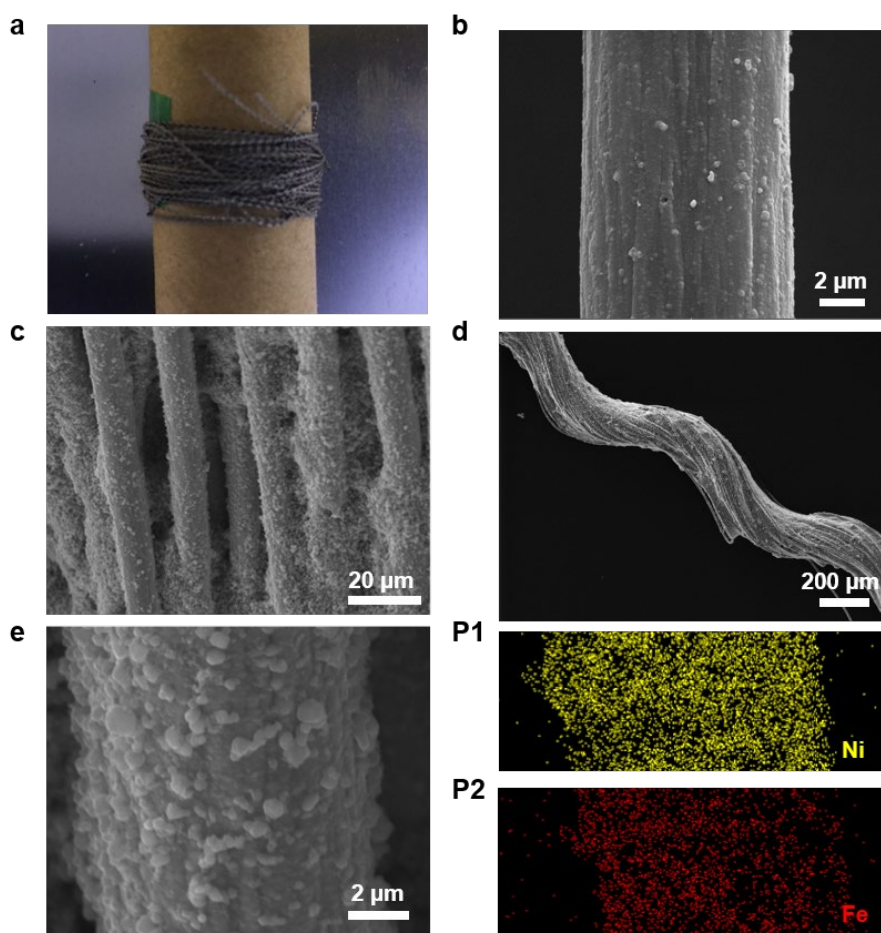
Figure S13. Characterizations of yarn-like cathodes. a) A scroll of nickel (Ni)-coated C (Ni-C) yarn. b) SEM image of a Ni-C fiber. c, d) SEM images of yarn-like LFP cathodes. e) SEM image of a lithium iron phosphate (LFP)-coated Ni-C fiber. The EDX mapping shows the distribution of Ni (P1) and iron (Fe) (P2).
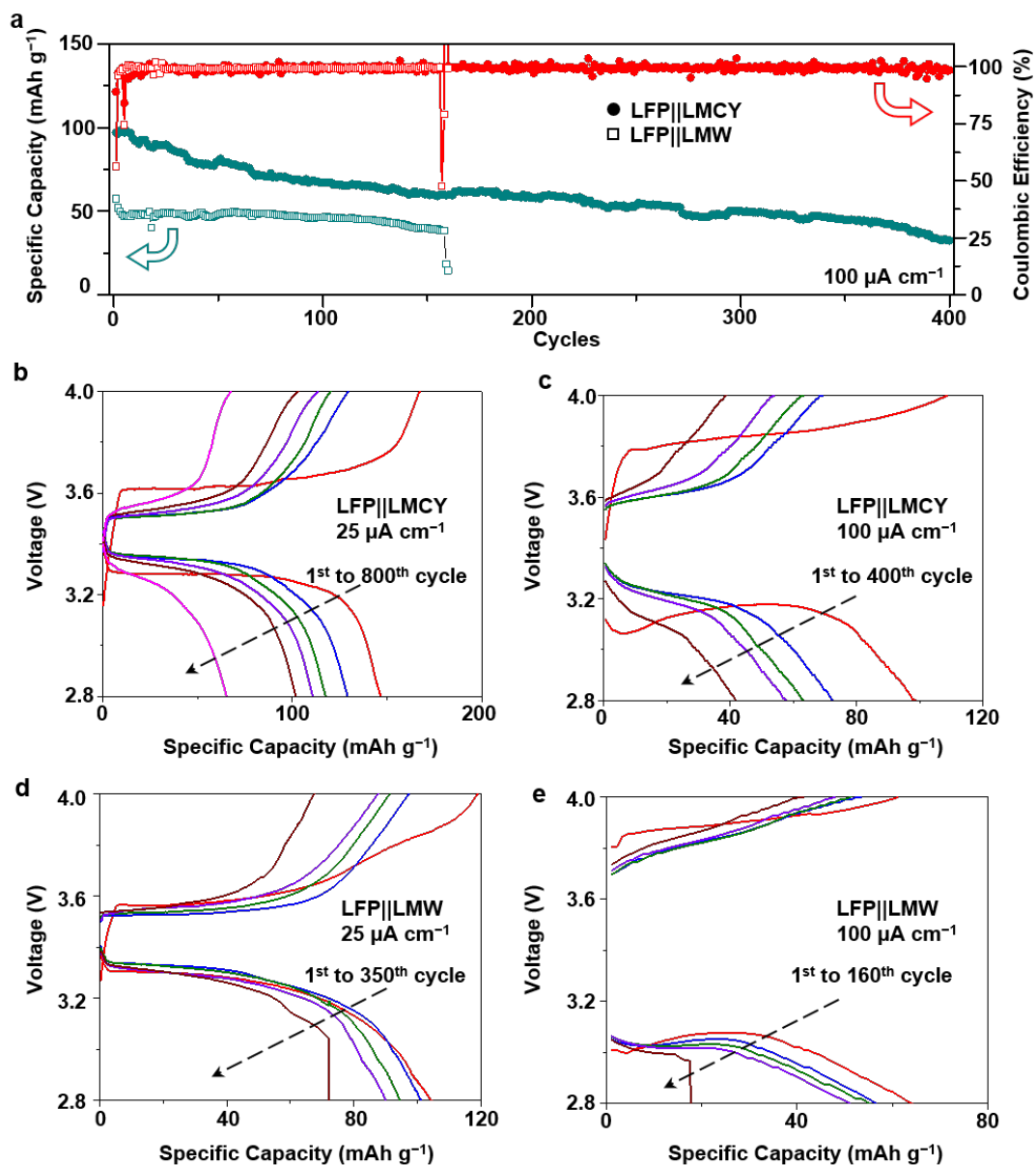
Figure S14. Electrochemical performances of LFP||LMCY and LFP||LMW batteries. a) Cycling performance of LFP||LMCY and LFP||LMW batteries tested at 100 μA cm⁻¹. b, c) Voltage profiles of LFP||LMCY tested at 25 μA cm⁻¹ and 100 μA cm⁻¹, respectively. d, e) Voltage profiles of LFP||LMW tested at 25 μA cm⁻¹ and 100 μA cm⁻¹, respectively.
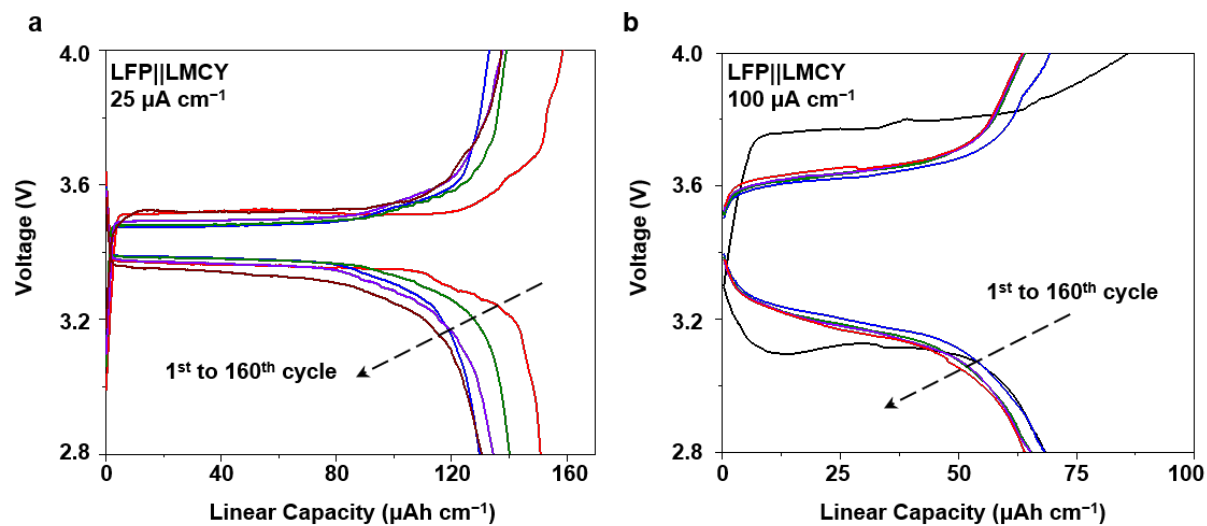
Figure S15. Electrochemical performances of LFP‖LMCY batteries with a high mass loading of LFP. a) Voltage profiles of LFP‖LMCY tested at 25 μA cm^{-1}. b) Voltage profiles of LFP‖LMCY tested at 100 μA cm^{-1}.
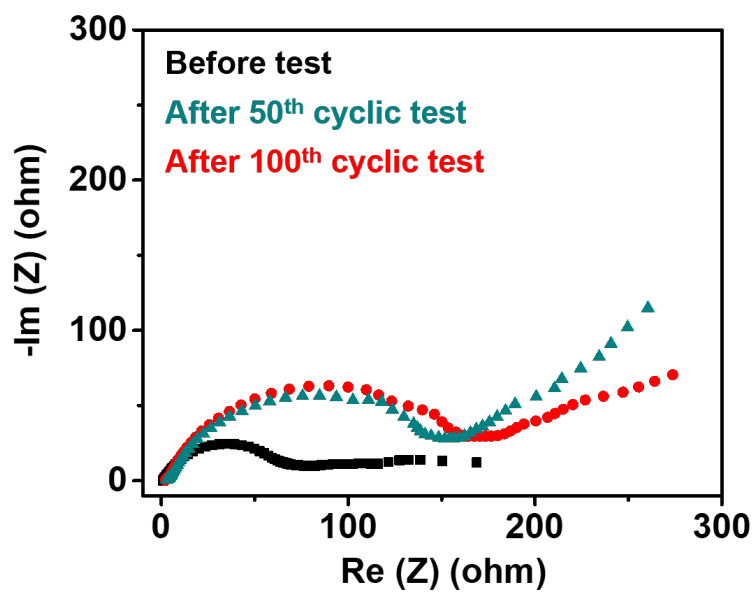
Figure S16. Electrochemical impedance test of LFP||LMCY batteries before and after cyclic
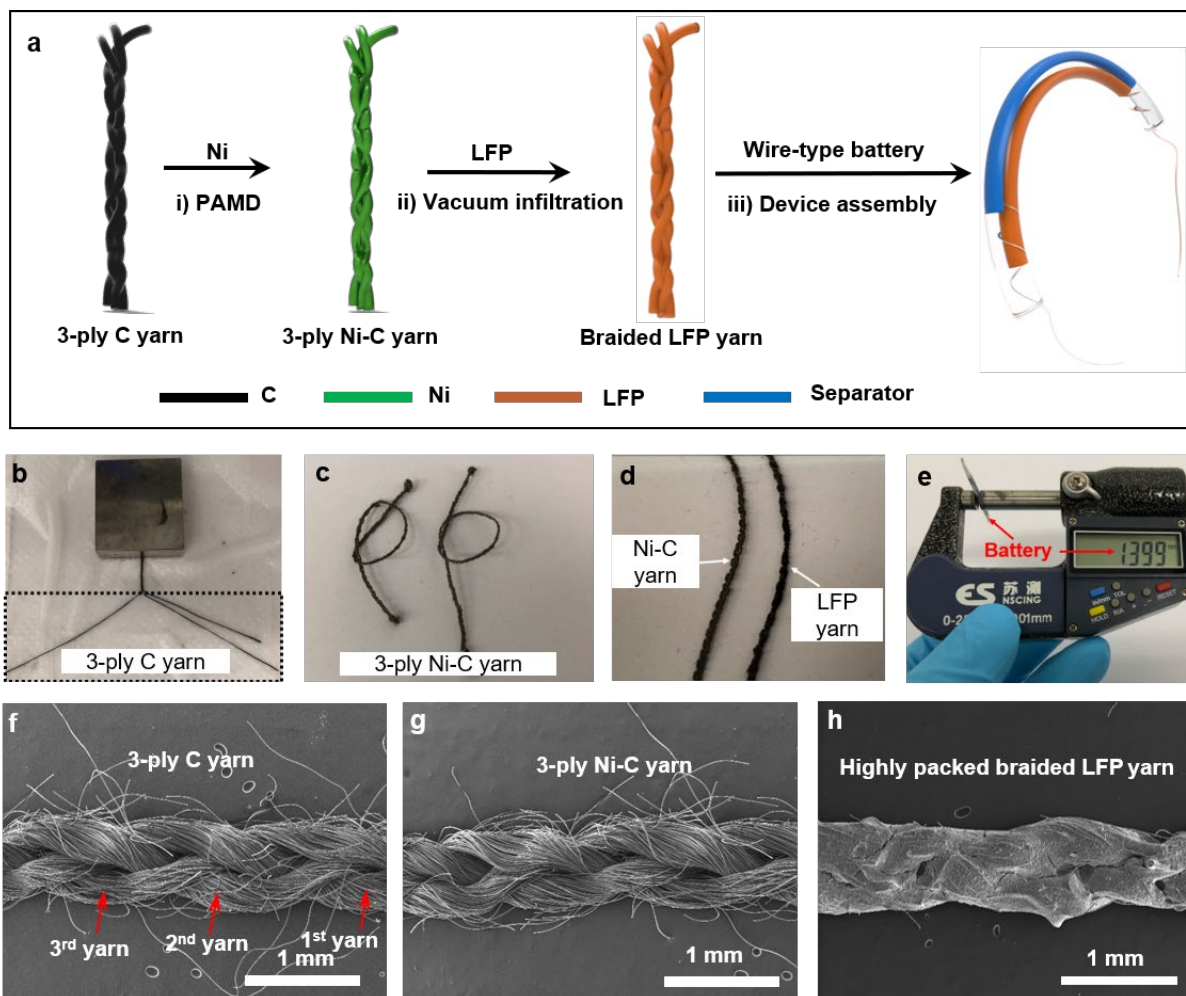
test.

Figure S17. LFP‖LMCY batteries using braided yarn-like cathodes. a) Schematic illustration of the fabrication of LFP‖LMCY using braided yarn-like cathodes. b-e) Digital images of braided three-ply C yarn, Ni-C yarn, LFP cathode yarn, as well as the resultant LFP‖LMCY. f-h) SEM images of three-ply C yarn, Ni-C yarn, and LFP cathode yarn.
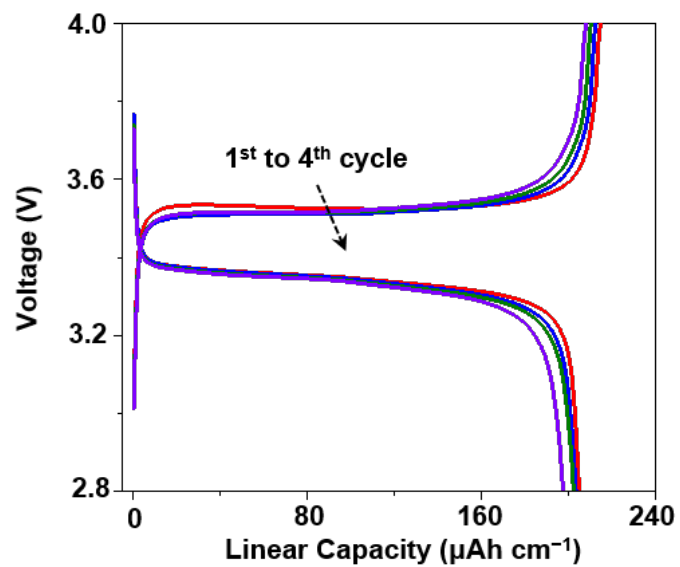
Figure S18. Electrochemical performance of LFP||LMCY using braided LFP cathode yarn.
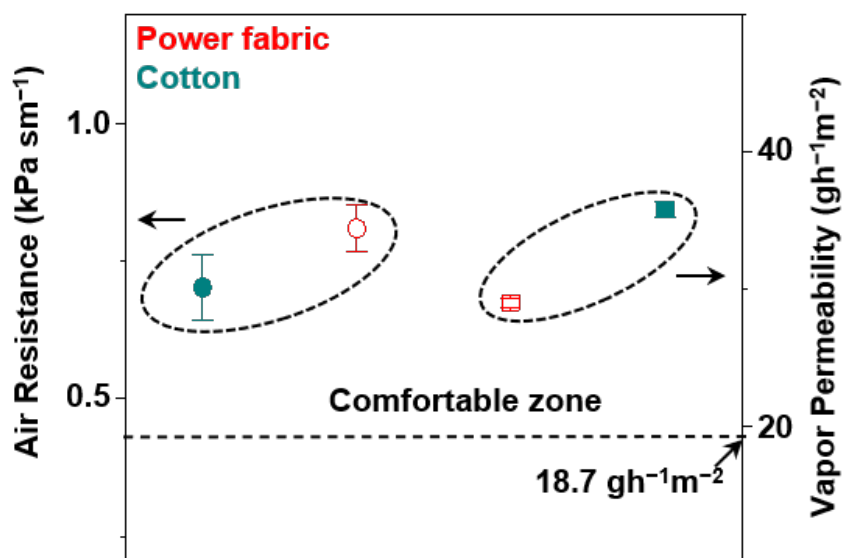
Figure S19. Comparison of air resistance and water vapor permeability between the as-fabricated battery textile (red) and commercial cotton (cyan). The power fabric shows similar air resistance and water vapor permeability with commercial cotton, which demonstrates its good wearing comfortability.
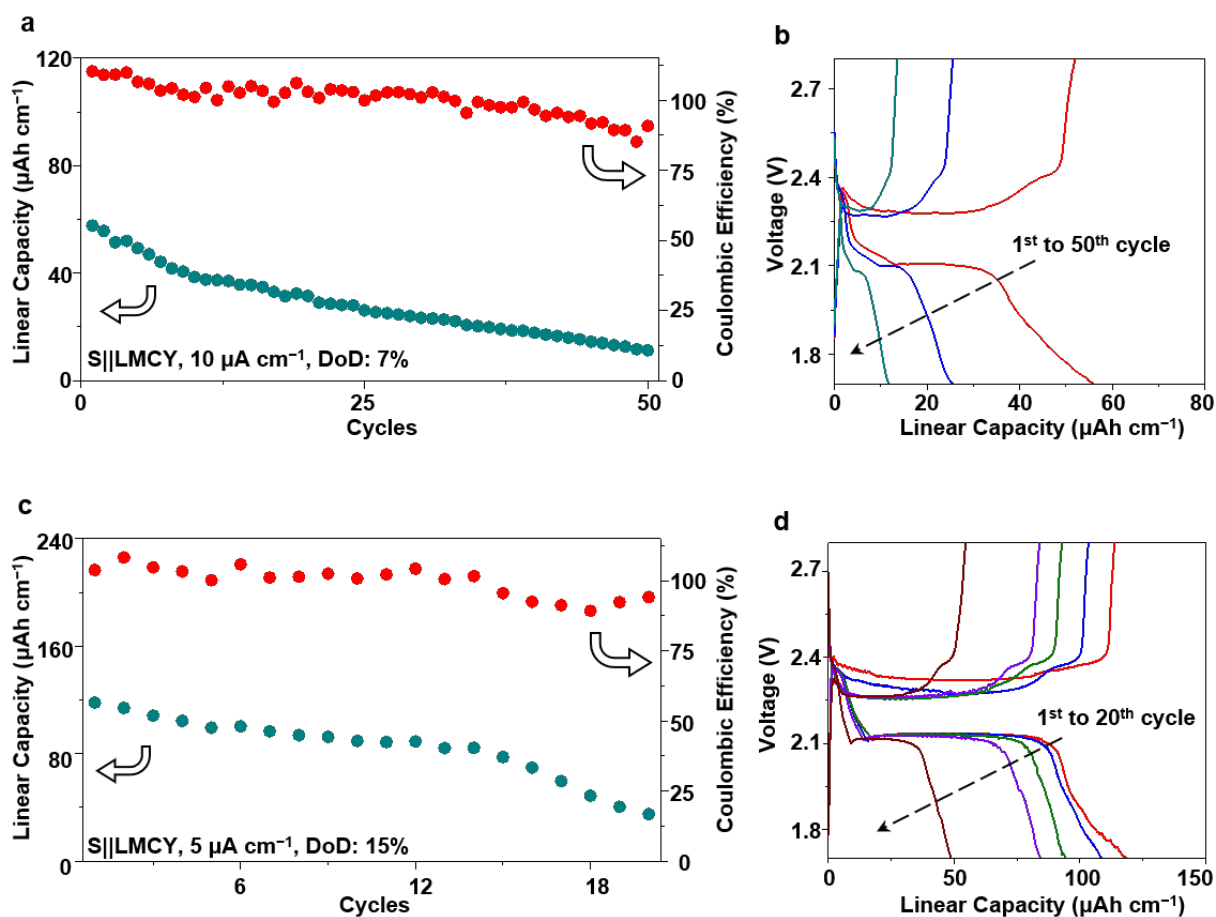
Figure S20. Electrochemical performances of S||LMCY batteries. a, b) Cycling performance and voltage profiles of S||LMCY tested at a DoD of 7% and a current density of 10 μA cm⁻¹. c, d) Cycling performance and voltage profiles of S||LMCY tested at a DoD of 15% and a current density of 5 μA cm⁻¹.
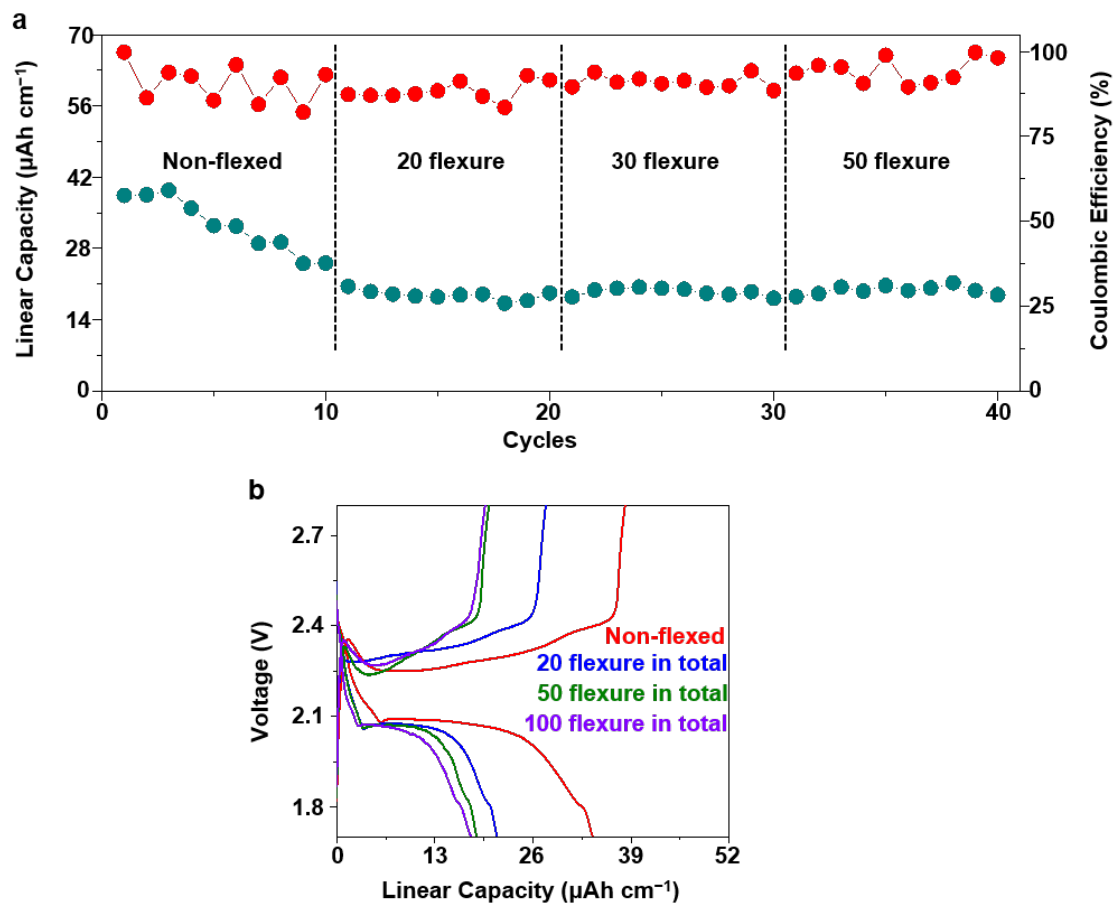
Figure S21. Flexibility of the S‖LMCY battery. a) 40 cycling tests are carried out during 100 flexure of the S‖LMCY. The capacity decay during the initial ten cycling tests comes from the irreversible dissolution of soluble lithium polysulfides (Li_2S_n, $n \geq 4$). b) Voltage profiles of S‖LMCY before and after bending for different cycles.

Table S1. Performance benchmark with state-of-the-art wire-type batteries.

Battery type	Voltage (V)	Initial capacity[a] (mAh g^{-1})	Cycles	Current density	Retention (%)	Energy density (Wh L^{-1}/Wh kg^{-1})
S‖Li wire [21]	2.1	762	3	0.1 C	65.6	20.4[b]/720[c]
S‖Li wire [43]	2.1	1117	100	0.1 C	30	0.9[b]/NA
O_2‖Li stick [23]	2.7	500	90	0.1 mA cm^{-1}	74.1	1.72[b]/NA
O_2‖Li wire [22]	2.45	500	100	0.28 mA cm^{-1}	81.6	26.2[b]/2457[c]
CO_2‖Li wire [24]	3.4	NA	40	$8*10^{-2}$ mA cm^{-2}	NA	70[b]/117[b]
MoS_2‖Li@CNT [31]	1.9	1176	100	$3.1*10^{-5}$ mA cm^{-1}	96	5.7[b]/11.9[c]
$LiMn_2O_4$‖TiO_2 [40]	1.5	168	100	$5.6*10^{-3}$ mA cm^{-1}	79.3	NA/NA
$LiCoO_2$‖Sn [15]	3.5	740	8	0.1 mA cm^{-1}	87	133.59[b]/NA
$LiMn_2O_4$‖$Li_4Ti_5O_{12}$ [13]	2.5	138	100	$5*10^{-2}$ mA cm^{-1}	85	17.7[b]/27[b]
C‖Al [44]	4	145	200	1 C	80	10.4[b]/173.3[b]
Ag_2O‖Zn [12]	1.5	NA	100	0.5 C	94	72.2[b]/NA
MnO_2‖Zn [51]	1.5	302.1	500	2 A g^{-1}	98.5	53.8[b]/NA
O_2‖Zn [14]	0.9	12470	20	1 A g^{-1}	NA	5.7[b]/NA
O_2‖Zn [46]	1.1	550	75	$4.7*10^{-2}$ mA cm^{-1}	NA	36.1[b]/649[c]
MnO_2‖Zn [52]	1.4	NA	200	0.5 C	75	162.5[b]/NA
$Na_{0.44}MnO_2$‖$NaTi_2(PO_4)_3$ [45]	1.1	46	100	0.1 A g^{-1}	76	25.7[b]/NA
LFP‖LMCY (This work)	**3.4**	**150**	**800**	**$2.5*10^{-2}$ mA cm^{-1}**	**42**	**70.5[b]/110.3[b]**
LFP‖LMCY (This work)	**3.4**	**101**	**400**	**0.1 mA cm^{-1}**	**34**	**90.5[b]/122.1[b]**
LFP‖LMCY (This work)	**3.4**	**126**	**170**	**$2.5*10^{-2}$ mA cm^{-1}**	**88**	**292.4[b]/244.3[b]**
LFP‖LMCY (This work)	**3.4**	**85**	**170**	**0.1 mA cm^{-1}**	**92**	**122.4[b]/136.6[b]**

[a] Initial capacity is calculated based on the mass loading of active materials.

[b] Energy density is calculated based on the weight/volume of the whole battery w/o package.

[c] Energy density is calculated based on the weight/volume of one of the electrode (cathode/anode).

Table S2. Simulation parameters.

Material and property	Li fiber	Cu-C fiber
Elastic modulus (GPa)	74	180
Poisson ratio	0.3	0.25
Yield modulus (GPa)	1.2	NA
Work hardening exponent	0.15	NA
Cut-off stress (GPa)	2.1	NA